



A lightweight convolutional neural network with end-to-end learning for three-dimensional mineral prospectivity modeling: A case study of the Sanhetun Area, Heilongjiang Province, Northeastern China

Baoyi Zhang ^a, Kun Xu ^a, Umair Khan ^{b,*}, Xuefeng Li ^c, Linze Du ^a, Zhanghao Xu ^a

^a Key Laboratory of Metallogenetic Prediction of Nonferrous Metals and Geological Environment Monitoring (Ministry of Education), School of Geosciences and Info-Physics, Central South University, Changsha 410083, China

^b Institute of Deep-Sea Science and Engineering, Chinese Academy of Sciences, Sanya 572000, China

^c Heilongjiang Institute of Natural Resources Survey, Haerbin 150094, China

ARTICLE INFO

Keywords:

3D geological models
Convolutional neural networks
Deconvolution
Weight of evidence
3D mineral prospectivity modeling

ABSTRACT

With the continuous exploitation of surface and shallow mineral resources, the global demand for concealed ore deposit exploration is increasing. However, concealed mineral prospectivity modeling (MPM) requires significant efforts, particularly in terms of methods and technologies for three-dimensional modeling. In this study, we propose a lightweight three-dimensional convolutional neural network (3D CNN) for MPM, which adopts the inception structure of GoogleNet and combines the idea of end-to-end learning. We replace the fully connected layer in the conventional CNN with deconvolution, which can greatly reduce the required parameters during the training process and accelerate the convergence. The proposed method overcomes the disadvantage that other shallow machine learning methods cannot extract spatial neighborhood information, while it can extract cross-correlations among geological factors and generates less parameters by a lightweight network when facing massive data. Additionally, compared with the patch-wise method commonly used in previous studies, we use the pixel-wise method for end-to-end learning, which not only overcomes the drawbacks of random sampling but also considers the influence of each voxel when calculating the loss function. The three-dimensional multi-source geoscientific characteristics obtained from the geophysical inversion and 3D geological models are not discretized in order to promote effective CNN training while facilitating the ore-controlling representation. Comparing the predicted results between the 3D weight of evidence (WofE) and our proposed 3D CNN method for MPM, our proposed method and WofE delineated 100% of the known mineralization in high-favorability areas with voxel numbers of 70% and 95%, respectively. A case study of a structure-controlled hydrothermal gold deposit in the Sanhetun area of Heilongjiang Province demonstrates that the proposed 3D CNN method performs better than WofE in terms of prediction effectiveness and efficiency and effectively reveals the correlation between mineralization and adjacent ore-controlling characteristics. Moreover, the proposed 3D CNN method can simulate non-linear metallogenic processes and mine hidden relationships to reveal complex ore-controlling characteristics. In conclusion, the proposed 3D CNN method can reduce the exploration effort in 3D MPM, thus greatly improving the efficiency of discovering concealed ore deposits.

1. Introduction

Three-dimensional mineral prospectivity modeling (3D MPM) is a quantitative approach used to delineate concealed orebodies from multi-

source, multiscale, and multi-dimensional geoscientific spatial datasets (Li et al., 2015; Mohammadpour et al., 2021; Li et al., 2023). Therefore, 3D MPM aims to describe the 3D spatial distribution and evolutionary relationship of geological units through integrating multivariate,

Abbreviations: MPM, Mineral prospectivity modeling; 3D CNN, Three-dimensional convolutional neural network; WofE, Weight of evidence; CAOB, Central Asian Orogenic Belt; FC, Fully connected; ReLU, Rectified linear unit; BN, Batch normalization; ROC, Receiver Operating Characteristic; AUC, Area under the ROC curve; MYI, Youden index.

* Corresponding author.

E-mail address: umairkhanbk@-mails.ucas.ac.cn (U. Khan).

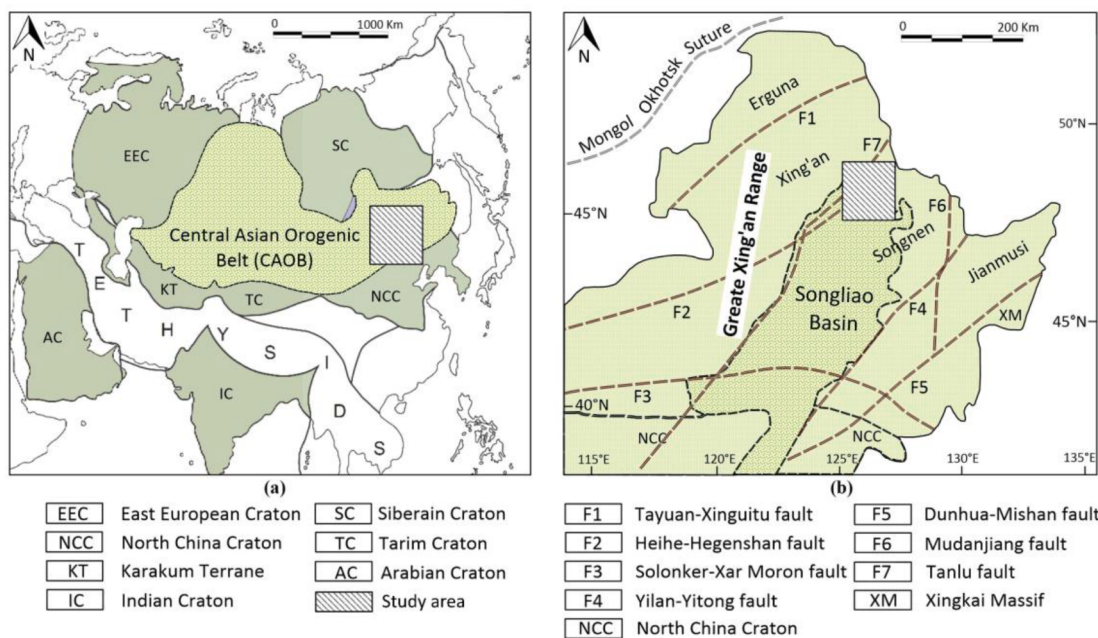


Fig. 1. (a) Tectonic division of NE Asia; and (b) Tectonic map of NE China.

massive, and heterogeneous multi-source geoscientific data (Zhang et al., 2018; Xu et al., 2021; Deng et al., 2022). Information of geological evolution, sub-surface geological structure, and mineralization is contained in geospatial data sets (Bérubé et al., 2018; Li et al., 2018; He et al., 2021). Three-dimensional MPM has become a useful tool for analyzing ore-forming environments, extracting effective ore-controlling factors, and describing real ore-forming processes (Rezaei et al., 2022). Therein, weight of evidence (WoFE) is a common 3D MPM method (Wang et al., 2015; Farahbakhsh et al., 2020), which uses conditional probability theory to evaluate the spatial cross-correlation between ore body and ore-controlling factors (Agterberg, 1991). The joint conditional independence between factors is a basic assumption of WoFE; however, various complex correlations between ore-controlling factors can lead to the failure of WoFE (Wang et al., 2011; Li et al., 2019). Furthermore, WoFE only can extract statistical correlations between known deposits and ore-controlling factors, while it is challenging for WoFE to characterize the spatial auto- and cross-correlations between known deposits and ore-controlling factors.

Recent advancements have introduced various machine learning approaches into 3D MPM. While support vector machines (SVMs) can theoretically transform linearly indistinguishable samples into linearly distinguishable ones, practical implementation with large-scale training samples poses challenges (Fu et al., 2021). Decision tree-based ensemble machine learning approaches, e.g., random forests (RFs) (Xiang et al., 2019; Qin et al., 2021), extreme gradient boosting (XGBoost) (Zhang et al., 2022), and light gradient boosting machine (LightGBM) (Li et al., 2023), although less affected by category imbalance, overlook cross-correlation between different attributes in the dataset. Deep learning methodologies, particularly convolutional neural networks (CNNs) (Lecun et al., 1998), have made significant strides in various scientific domains (LeCun et al., 2015). These methods excel in learning hierarchical representations of input characteristics through multiple levels of abstraction. Applying deep learning to delineate metallogenic prospects holds promise for comprehending mineralization across different spatial scales. Recent studies have demonstrated the efficacy of deep learning, particularly CNNs, in addressing the challenges faced by traditional MPM methods like WoFE in complex metallogenic conditions (Zuo et al., 2019; Ghezelbash et al., 2020; Zhang et al., 2021). CNNs not only capture auto-correlations within a massive 3D block model but also extract cross-correlations across multiple characteristic dimensions, allowing

them to leverage spatial auto-auto-correlations and characteristic cross-correlations for improved classification models (Zuo and Xiong, 2017; Li, H et al., 2020). Deng et al. (2022) and Zheng et al. (2023) have proposed a 3D MPM method that employs 2D CNNs to construct deep networks for building prospectivity model, thereby understanding intricate cross-correlations between the localization of mineralization and the compiled geometry of geological boundaries. In a comparative experiment with WoFE, Li et al. (2021) found a 3D CNN model to more effective in mining the correlation between data in the Huayuan sedimentary Mn deposit, China. Additionally, Li et al. (2023) utilized 3D CNNs based on a LeNet-5 backbone network, featuring seven network structure layers, to identify highly prospective areas for mineralization within the Chating area, China. However, previous studies have typically used well-established CNN structures in mineralization feature extraction. Consequently, there is a large number of parameters to be estimated during the training process, which takes a lot of time associated with the use of 3D CNNs with deep network structures.

In this study, our emphasis lies on addressing the time-saving of deep 3D CNN structures, enabling the extraction of spatial nonlinear characteristics and cross-correlations between ore-controlling factors from a vast amount of 3D voxels. We use GoogleNet's inception unit combined with deconvolution to greatly reduce memory consumption and save time costs, while maintaining the performance of the CNN network. The prospectivity modeling with CNNs, involving fusing spatial neighborhood characteristics, cross-correlations between ore-controlling factors and introducing non-linear layers, was implemented considering the 3D characteristic models of multiple geospatial data for the Sanhetun area of Heilongjiang Province, Northeastern China. The experimental results demonstrate that the proposed model can better model the complex distribution of mineralization in the study area, thus providing effective decision support for mineral exploration engineering design.

2. Study area and dataset

2.1. Geological

The Lesser Hinggan Range is located in the Central Asian Orogenic Belt (CAOB); see Fig. 1a. The CAOB has been documented as the largest Phanerozoic accretionary orogen and the most-researched orogenic belt in the world, having high significance in terms of continental accretion

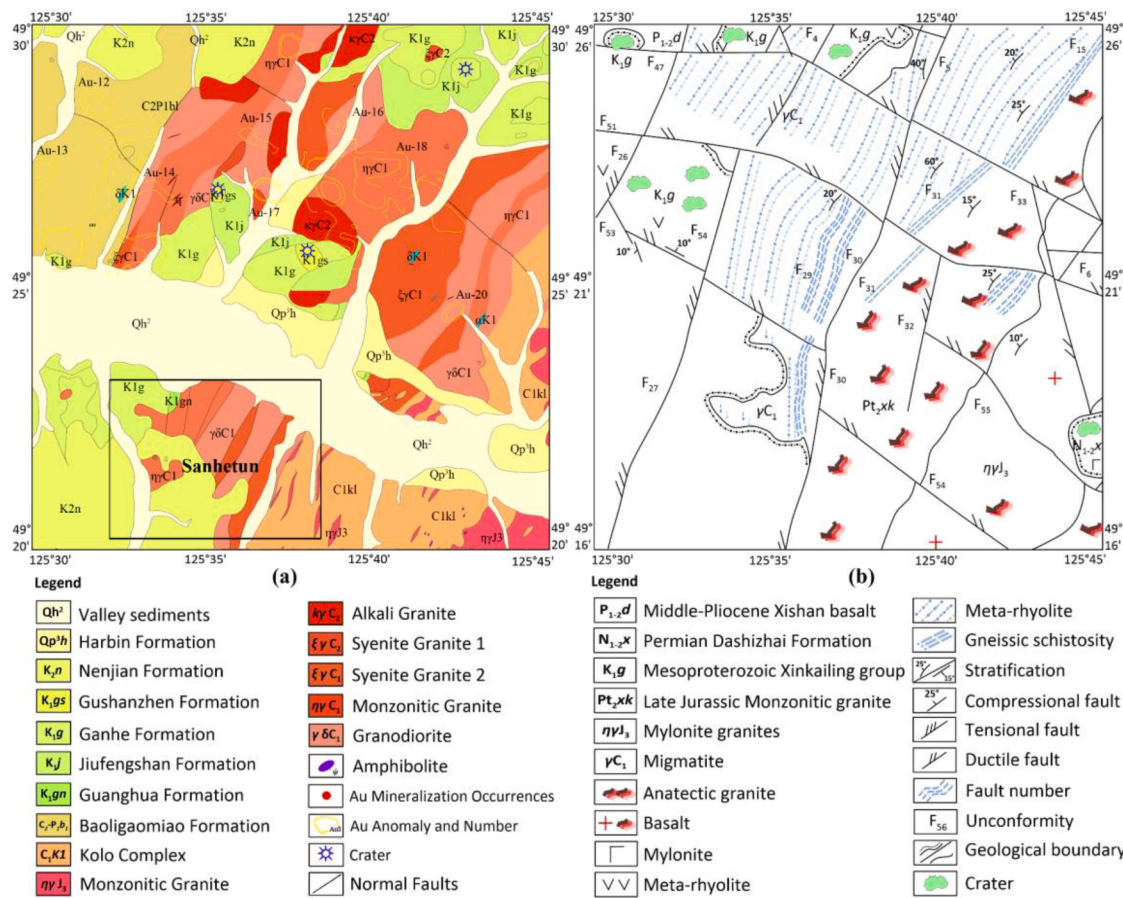


Fig. 2. Schematic (a) geological and (b) structural maps of the Sanhetun area and adjacent area in Heilongjiang Province, NE China.

and ore formation (Liu et al., 2017; Wang et al., 2018; Zhang et al., 2019) (Fig. 1b). In the Lesser Hinggan Range, a lot of epithermal gold deposits, e.g., the Dong'an (Zhang et al., 2010), Tuanjieguo (Wang et al., 2006), Sandaowan (Liu et al., 2011), and Gaosongshan deposits (Hao et al., 2016), have been discovered. Therefore, the region is considered as a prospective region for gold deposits with favorable mineralization in China. The altered zone along the fault is one of the key characteristics of the Lesser Hinggan Range-type deposits.

The Sanhetun area is located in the north Lesser Hinggan Range (Fig. 2a). The major lithological units in the study area consist of intrusive rock, volcanic rock, metamorphic rock, and vein rock, which are generally separated by the NNE- and NW-trending fault zones (Fig. 2b). The intrusive rock is composed of the Early carboniferous and Early Jurassic anatexic granite, which has guiding significance for gold and copper deposit exploration. The formation of volcanic rock is inherently associated with the volcanic magmatism in the Guanghua and Ganhe periods, in which the ore-forming fluid related to volcanic rocks migrated along fractures and fissures, forming volcanic hydrothermal and medium-low temperature hydrothermal gold deposits under favorable physical and chemical conditions. A NE-SN compression and subsequent extensional stress associated with the reorganization of the subducting Pacific Plate configuration promoted the generation of metamorphic rock, which mainly consists of mylonite, tectonic schist, leptynites, leptites, and amphibolite. The vein rock was formed in the Early Carboniferous granitic mylonite, and their types are diorite porphyrite and andesite, respectively.

In the study area, hydrothermal mineralization activities occur in the NNE- and NW-trending faults, which display clear abnormal development of gold and silver in soil, mainly consisting of mylonitic granite silicified and pyrite alteration. The predominant processes of alteration are structural controls and volcanic activities. The major structural

controls essentially resulted in structural deformation, driving fluid flows, trapping ore-forming fluids, and/or metal deposition in fault zones under conditions of fluctuating pressure and rock permeability. The significant volcanic activities essentially resulted in destroying existing geological bodies and local enrichment of gold elements.

2.2. Mineralization

The formation of deposits in the study area and its adjacent area of the Duobaoshan–Daxintun is closely related to fault zones. The deposits occurring during the Hercynian and Yanshanian periods exhibit the following sedimentary characteristics: The deposits during the Hercynian period are mainly hosted in the NW-trending faults and folds (e.g., the Duobaoshan copper deposit and the Tongshan copper-molybdenum deposit), and the deposits during the Yanshanian period are controlled by the NE-trending faults (e.g., the Pangkaimen gold deposit, the Kuanhe gold deposit, and the Zhengguang gold deposit). In addition, frequent large-scale multi-phase hydrothermal activities provided favorable ore-forming conditions. The types of hydrothermal deposit in the Greater Khingan Range include: 1) Porphyry-hydrothermal deposits, represented by large copper deposits in the Duobaoshan and Tongshan deposits; 2) contact metasomatic deposits, represented by the Sankuangou iron-copper deposit and Guanniaohe scheelite deposit; 3) volcanic hydrothermal deposits, represented by the Pangkaimen medium-sized silver-gold deposits; and 4) low-moderate temperature pyrometasomatic filling quartz vein-type deposits, represented by the Kuanhe and Sandaowanzi gold deposits (Fig. 3) (Liu et al., 2017; Deng et al., 2018; Zhang et al., 2021).

In the study area, gold mineralization is mainly hosted in the Early Carboniferous granitic mylonite near the Lower Cretaceous Ganhe Formation. The protolith spectra show that the gold content of the Ganhe

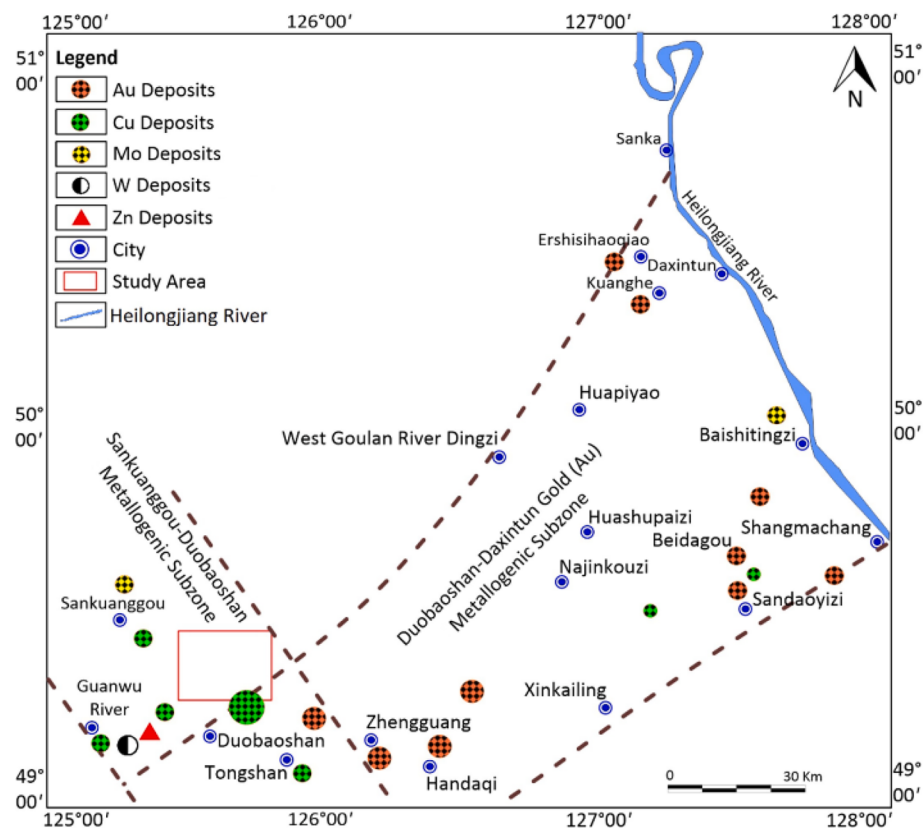


Fig. 3. Large- to medium-sized Au, Cu, Mo, W, and Zn deposits in the region.

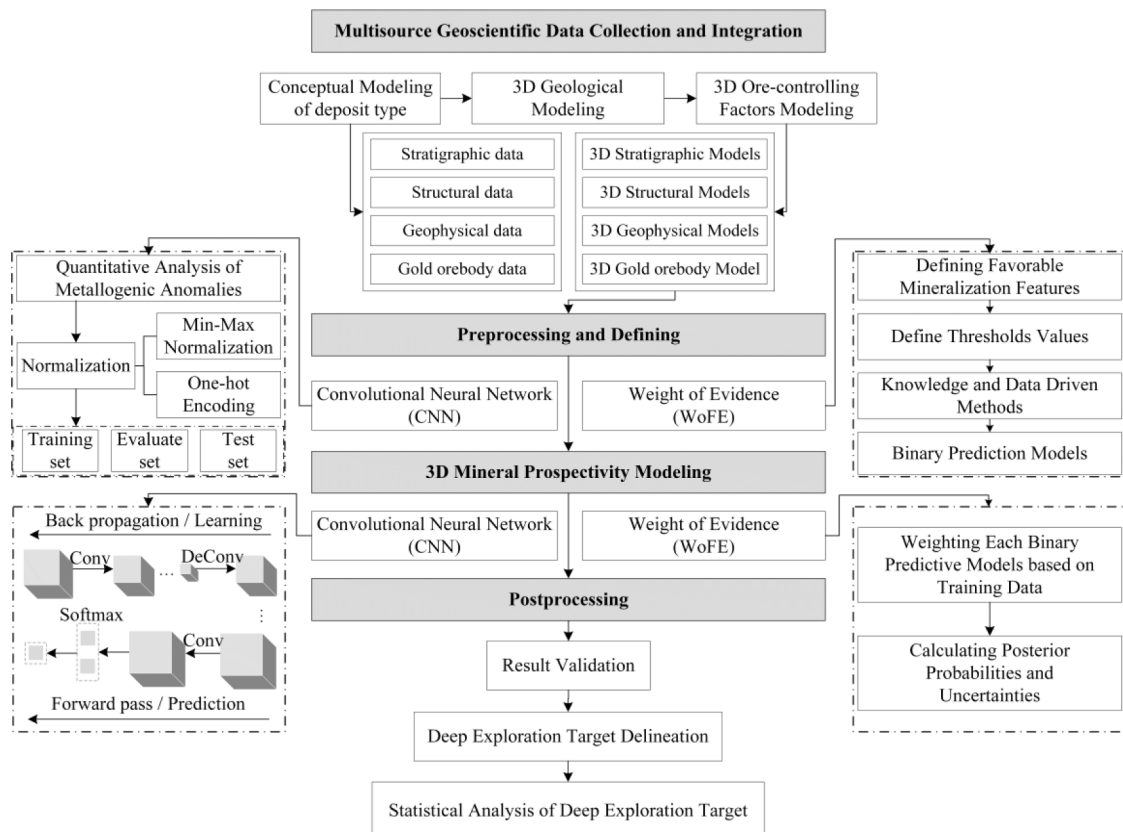


Fig. 4. Flowchart of the 3D mineral prospectivity modeling approach followed in this study.

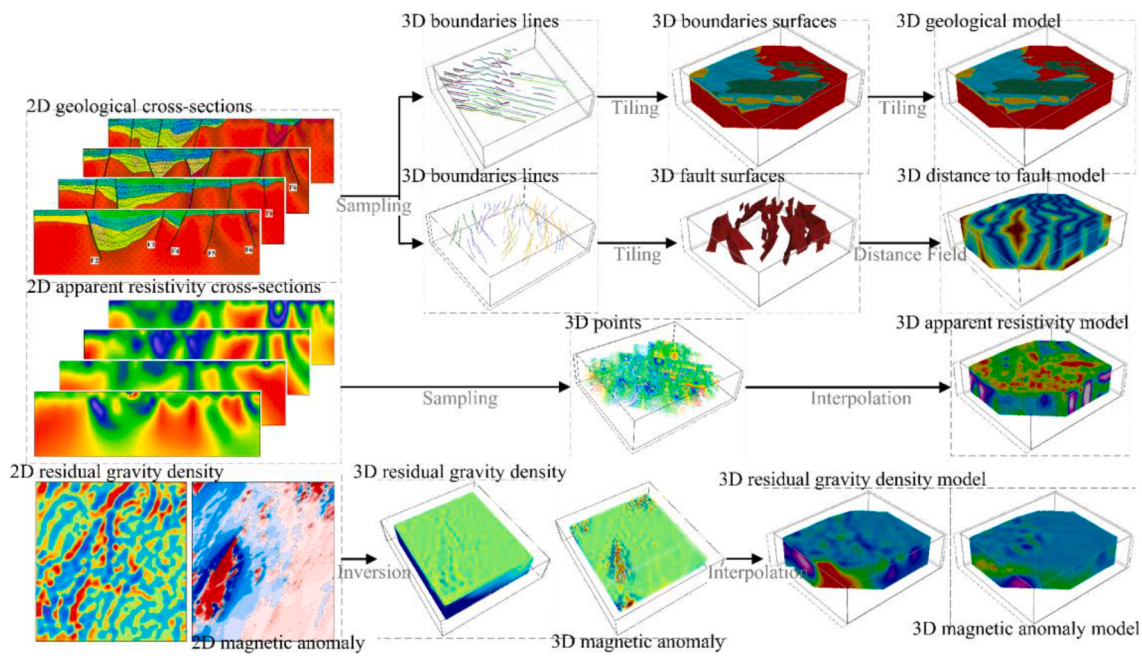


Fig. 5. Flowchart of the 3D geoscientific modeling.

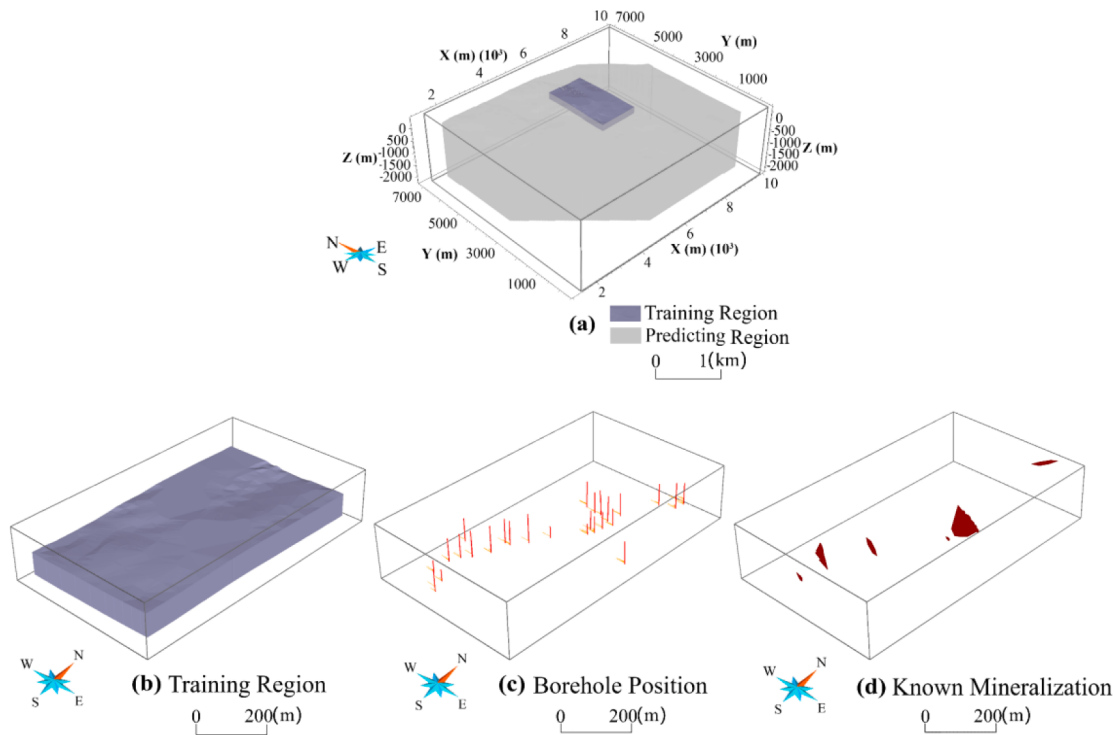


Fig. 6. (a) Training and prediction region; (b) training region; (c) boreholes; and (d) known gold orebodies.

Formation near the contact zone is obviously high, and part of it reaches the mineralized body, indicating that the volcanic magma eruptions carried a large amount of gold components when forming the rock. The Late Carboniferous tectonic activity led to the upwelling localization of large-scale granitic magma in the region, which migrated and enriched gold elements. Under the effect of the Early–Middle Jurassic Mongolian–Okhotsk Ocean closure and the two-way subduction of the Izenaiji plate to the East Asian continent, the regional thermodynamic metamorphism deformed the Early Carboniferous granites in the study area

through ductile metamorphism. High temperature and high pressure caused recrystallization of granite minerals, and ductile shear caused gold elements to further migrate and enrich. During the Early Cretaceous Ganhe period, volcanic eruption under continental rift tension not only carried a lot of gold and other useful mineralized components, but also further activated and migrated the gold and other mineralized elements enriched in the early geological body under the influence of the high temperature. On one hand, the multi-phase magmatism increased the solubility and salinity of fluid in the wall rocks (i.e., the

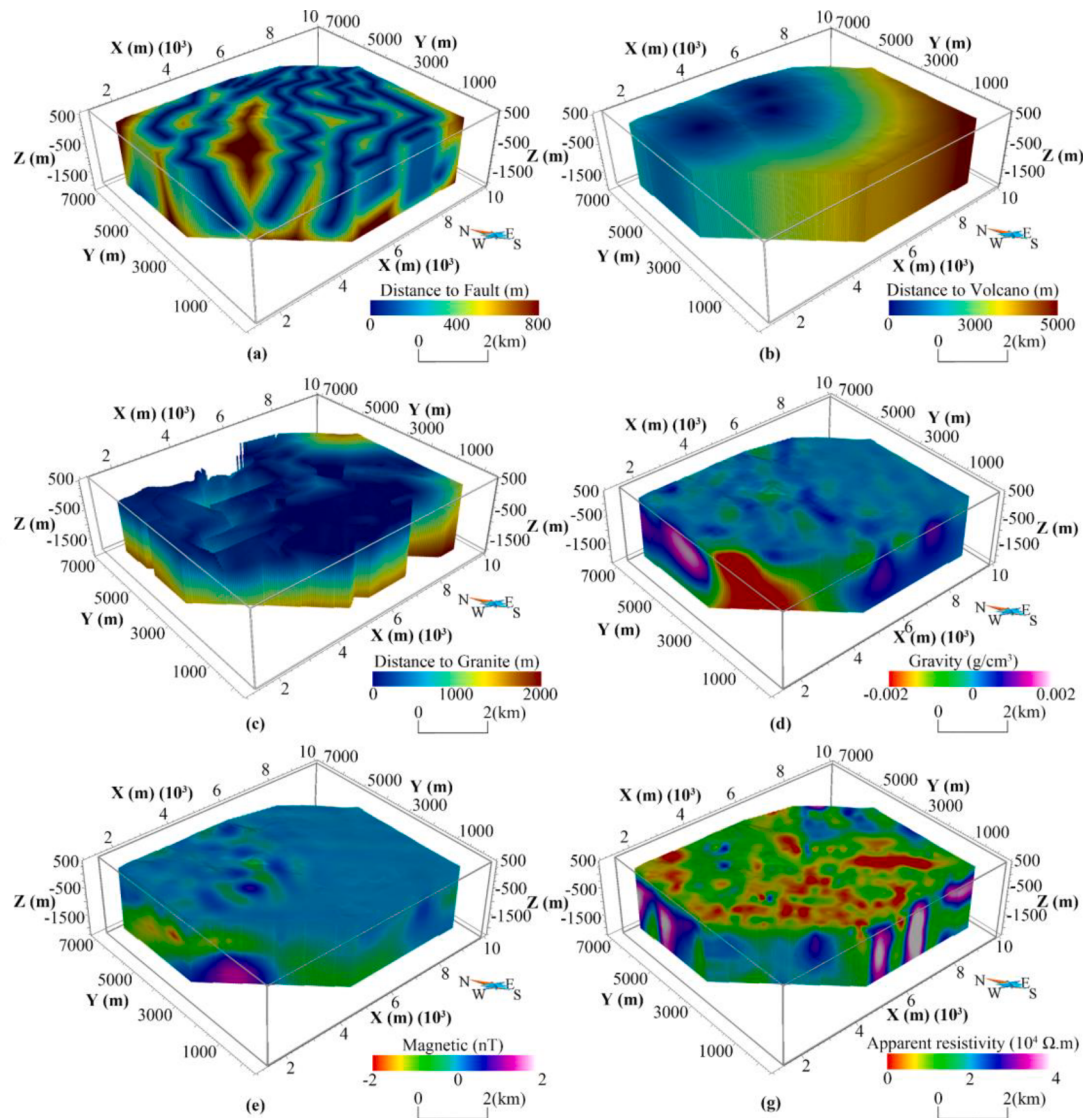


Fig. 7. 3D structural, stratigraphic, and geophysical ore-controlling factors: (a) Distance to fault; (b) distance to paleo-volcanic crater; (c) early Carboniferous granite complex interior distance to the Ganhe Formation; (d) residual gravitational density; (e) magnetic anomaly; and (f) apparent resistivity distribution.

Neoproterozoic Xinkailing Group and Augen Granitic Mylonite) after heating and, consequently, the solubility of gold increased sharply, prompting the activated transport of gold in the wall rocks. On the other hand, the hydrothermal fluid in the late magnetic period extracted the gold from the magma, which gradually transported, precipitated, and enriched the gold into favorable structural mineralization zones with the decrease in temperature.

2.3. Data set

To implement 3D MPM in the Sanhetun gold deposit, we collected a current and historical mineral exploration data set including a surface geological map (scale of 1:50,000), 13 geological cross-sections from 335 m to –2000 m, 13 apparent resistivity cross-sections, 27 drillholes, 1 outcrop, 2467 sample testing data of Ag and Au, 3D residual gravitational density data, and 3D magnetic anomaly data. Due to problems with numerous formats and inconsistent coordinate systems, data mining processing is required to extract the critical metallogenic information, to unify coordinate systems, and to subsequently convert different formats.

The geological and geophysical exploration data were used to build 3D models of the study area. First, the shapes of the fault and strata were

delineated, according to the geological cross-section profiles. The location of the paleo-volcanic craters was determined from the surface geological map. Thereafter, the available geological and geophysical data sets were used to construct 3D geological models (e.g., stratigraphic units, volcanic basins, and fault models) and 3D geophysical property models (e.g., apparent resistivity, residual gravitational density, and magnetic anomaly models). These multiple geoscientific models were then used to generate quantitative prospecting factors through spatial analysis in 3D space. The three-dimensional prospecting factors included the fault distance field, volcanic distance field, contact surface between the Ganhe Formation and the Early Carboniferous granite complex, apparent resistivity, residual gravitational density, and magnetic anomaly.

3. Methods

Fig. 4 provides an overview of our comprehensive 3D MPM methodology. This process comprises four key stages: 1) Individual lithologies, structures, and geological bodies were reconstructed using 3D geological modelling techniques; 2) 3D geological variable related to ore-controlling factors, e.g., lithology, alteration zone, geological structures, and geophysical properties, were characterized facilitated by

Table 1
Ore-controlling factors for gold prospecting in the Sanhetun area.

Ore-controlling Conditions	Metallogenic geological anomalies	Prospecting models
Stratigraphic	Early Carboniferous granite complex; the contact surface between the Early Carboniferous granite complex and the Ganhe Formation.	Early Carboniferous granite complex interior distance to the Ganhe Formation
Structural	Ductile shear zone Volcanic activity	Distance to fault Distance to paleo-volcanic crater
Geophysical	The high resistivity area; the contact zone of the low and weak positive and negative resistivity anomalies and the superposition of positive and negative anomalies. The low magnetic; the contact zone with low and weak positive and negative magnetic anomalies.	Apparent resistivity Magnetic anomaly
Orebodies	The high-density edge of the residual density anomalies Gold orebodies	Residual gravitational density Gold orebodies

employing 3D spatial analysis and geostatistics methodologies for both WofE and 3D CNNs; 3) The 3D MPM process was executed utilizing both CNNs and WofE approaches, and statistical metrics were subsequently employed to rigorously evaluate and compare the performances of these two approaches; and 4) The resulting deep prospecting targets generated by CNNs and WofE were delineated and overlaid onto the evidence factors to facilitate a detailed comparative analysis of the outcomes produced by the two distinct approaches.

3.1. Three-Dimensional geoscientific modeling

Three-dimensional geological modeling provides an essential tool for solving specific geological problems and studying geological evolution in the deep sub-surface. Furthermore, a 3D geological structural model may visually investigate the 3D spatial distribution and orientation of geological bodies as well as their evolutionary relationship (Jessell, 2001; Zhang et al., 2023). A 3D geological structural model is capable of combining with geophysical (Lindsay et al., 2012; Wellmann et al., 2017; de la Varga et al., 2019) and geochemical fields (Vollgger et al.,

2015; Zhang et al., 2018; Wang et al., 2019) for specific geological analysis, e.g., metallogenetic analysis (Basson et al., 2017; Li et al., 2019; Wang et al., 2019), groundwater management (Hassen et al., 2016), and reservoir characterization (Ali et al., 2021; Khan et al., 2021).

Based on several geological and geophysical datasets, we built 3D geoscientific models of the study area, including 3D geological structural models (target strata, faults, volcanic basins, and orebodies) and 3D geophysical attributes models (density, magnetic anomaly, and apparent resistivity), in order to evaluate the geological structure and geophysical framework for detailed follow-up mineral prospectivity studies (Fig. 5) (Li et al., 2018). The modeling depth was ascertained to be not deeper than -2000 m according to the available drillhole and geophysical exploration depth of the study area. Furthermore, a cubic model was used to realize 3D quantitative expression of the ore-controlling factors. Taking into the spatial scope, resolutions of geological factors, and computational capacity, we established the voxel length × width × height as 5 m × 5 m × 5 m. A total of six ore-controlling factors were initially chosen as the 3D evidence layers with assigned block properties for the Sanhetun gold deposit. By analyzing the cross-correlation of ore occurrences and variables extracted from 3D geological models, it is possible to quantitatively define ore-controlling factors (e.g., mineralized contacts or mineralization-associated faults), which can help to delineate high prospectivity areas for future mineral exploration.

The 3D geological modelling comprises digital representation the spatial and attribute characteristics of the geological bodies. Subsequently, we built 3D digital models of the gold orebodies (known mineralization; Fig. 6); structural, stratigraphic, and geophysical attribute models (Fig. 7); and extracted the ore-controlling factors (Table 1).

3.2. Three-dimensional CNN model

3.2.1. Architecture

There are two common training modes for 3D CNN image segmentation: Patch-wise training and pixel-wise training (Ao et al., 2022). A patch consists of multiple pixels, expressing the spatial correlation of a characteristic (Cirean et al., 2012); accordingly, a block consists of multiple voxels in 3D space. Patch-wise training (Fig. 8a) selects a part of the patches as a training set by random sampling, taking the center pixel of a patch as the pixel of interest, and the output is the predicted label of the center pixel by the learned features from the whole patch (Ganin and Lempitsky, 2014; Pinheiro and Collobert, 2014). As patches are allowed to be highly overlapped, it is easy to handle class

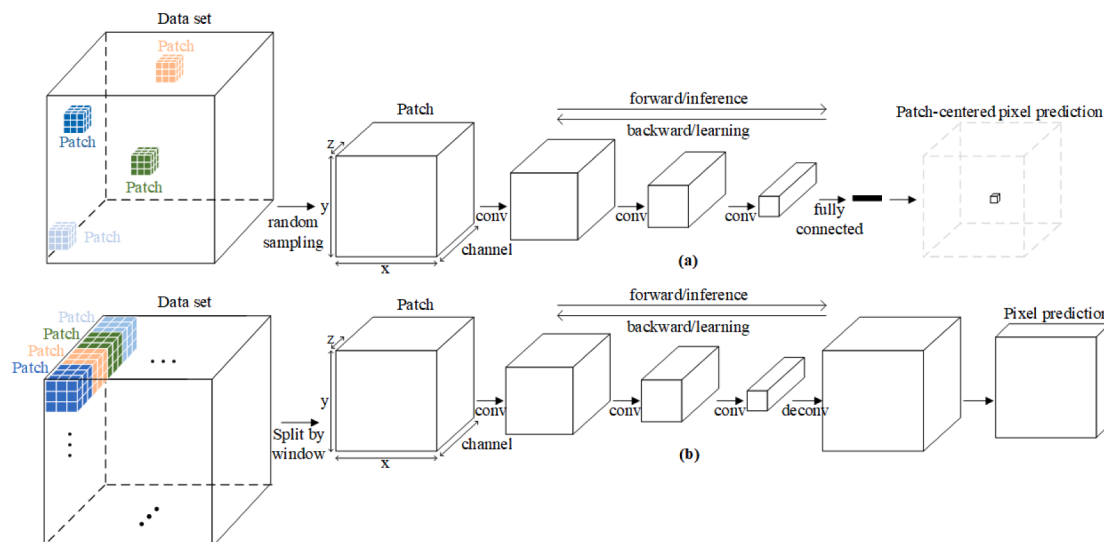


Fig. 8. The workflow of (a) patch-wise training, modified from (Le et al., 2013); and (b) pixel-wise training, modified from (Zhang et al., 2020).

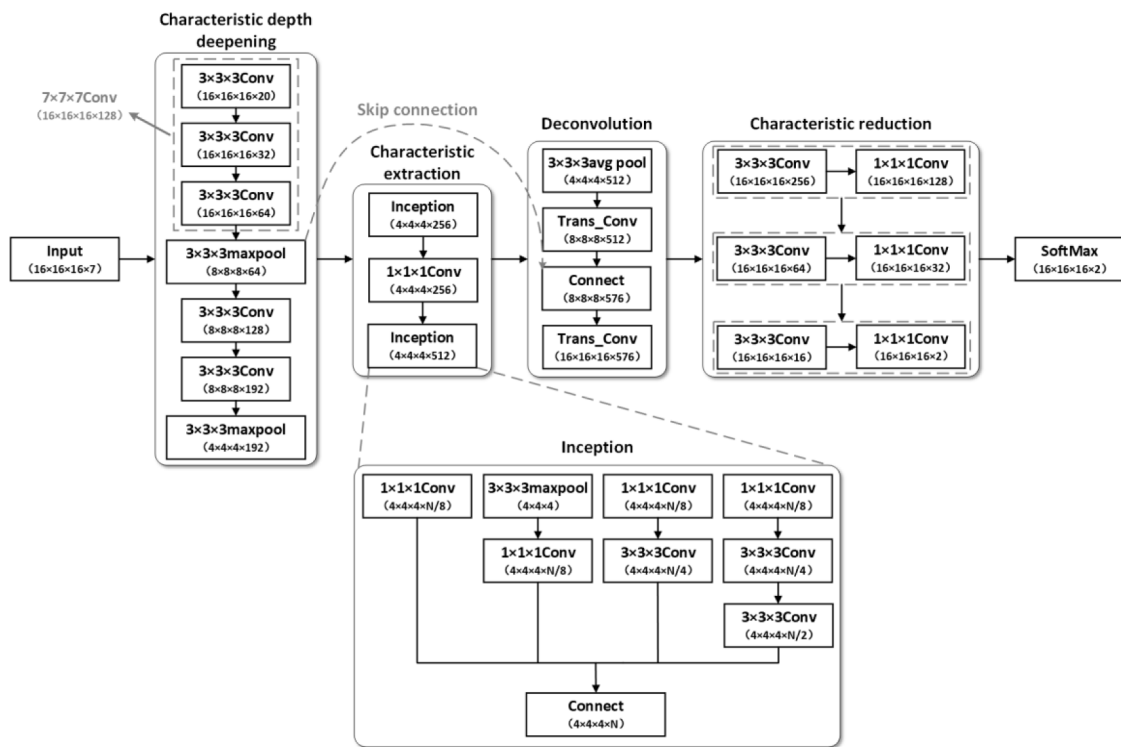


Fig. 9. The lightweight CNN architecture for classification of all voxels in the block.

Table 2
Comparison of the parameter counts of convolution layers.

Layer	Input	Output	Parameter	Sum
3 × 3 × 3Conv	16 × 16 × 16 × 11	16 × 16 × 16 × 20	5960	78,632
3 × 3 × 3Conv	16 × 16 × 16 × 20	16 × 16 × 16 × 32	17,312	
3 × 3 × 3Conv	16 × 16 × 16 × 32	16 × 16 × 16 × 64	55,360	
7 × 7 × 7Conv	16 × 16 × 16 × 64	16 × 16 × 16 × 128	120,768	120,768
3 × 3 × 3Conv	8 × 8 × 8 × 64	8 × 8 × 8 × 128	221,312	885,056
3 × 3 × 3Conv	8 × 8 × 8 × 128	8 × 8 × 8 × 192	663,744	
5 × 5 × 5Conv	8 × 8 × 8 × 64	8 × 8 × 8 × 192	1,536,192	1,536,192

imbalances; however, the spatial overlap between the training and test sets may hinder the generalization performance of the model. To prevent overfitting due to the high degree of patch similarity, training patches are usually randomly sampled, which cannot guarantee efficient and unbiased sampling (Lange et al., 2018; Zhang et al., 2020).

In contrast, pixel-wise training (Fig. 8b) obtains the label for each pixel in a patch after training, in which end-to-end learning can be achieved through back-propagation of per-pixel losses in the network using deconvolution. Pixel-wise training also incorporates spatial information from neighboring pixels during convolution and deconvolution processes. The loss function computes the sum of the losses of all labeled pixels in the output spatial map of the SoftMax layer, therefore, the gradients of all its pixel vectors are aggregated as its total gradient (Pinheiro and Collobert, 2014). As the receptive field of each pixel of the final patch layer is taken in a minibatch to ensure significant overlapping of the receptive fields, both feed-forward and backpropagation computations are much more efficient when calculated in a patch-by-patch manner over an entire space, instead of independently pixel-by-

Table 3
Number of parameters for end-to-end learning with deconvolution layers.

Part	Layer	Input	Output	Parameter	Sum
Deconvolution	3 × 3 × 3Deconv	4 × 4 × 512	8 × 8 × 512	7,078,400	20,288,018
Connect	8 × 8 × 512	8 × 8 × 576	–		
Characteristic reduction	3 × 3 × 3Conv	16 × 16 × 256	16 × 16 × 128	3,981,568	
1 × 1 × 1Conv	16 × 16 × 128	16 × 16 × 64	256		
3 × 3 × 3Conv	16 × 16 × 64	16 × 16 × 32	256	32,896	
1 × 1 × 1Conv	16 × 16 × 32	16 × 16 × 16	256		
3 × 3 × 3Conv	16 × 16 × 16	16 × 16 × 8	256	221,248	
1 × 1 × 1Conv	16 × 16 × 8	16 × 16 × 4	128		
3 × 3 × 3Conv	16 × 16 × 4	16 × 16 × 2	64	2080	
1 × 1 × 1Conv	16 × 16 × 2	16 × 16 × 1	32		
3 × 3 × 3Conv	16 × 16 × 1	16 × 16 × 1	32	13,840	
1 × 1 × 1Conv	16 × 16 × 1	16 × 16 × 1	34		

pixel (LeCun et al., 2012).

A 3D CNN generally consists of 3D convolutional, pooling, and fully connected layers, in order to retrieve characteristics and subsequently

Table 4

Number of parameters for the combination of the fully connected (FC) layers.

Layer	Input	Output	Parameter	Sum
FC layer	$4 \times 4 \times 4 \times 512$	4096×1	134,221,824	151,007,234
FC layer	4096×1	4096×1	16,781,312	
FC layer	4096×1	2×1	8194	

generate a classification probability by a SoftMax layer. Furthermore, each layer contains a certain number of channels, each of which represents a different feature. In the 3D CNN, convolution and pooling employ 3D characteristic blocks. The entire network structure used in this study can be divided into five parts (Fig. 9): the first part serves as an input layer with seven channels, where the patch size is set as $16 \times 16 \times 16$ according to the computational capacity; the second part is a combination of convolutional and pooling layers to increase the characteristic's channel depth; the third part is two inception structures to extract characteristics at different scales; the fourth part restores the block size using skip connection and deconvolution; the fifth part reduces the channels using $3 \times 3 \times 3$ and $1 \times 1 \times 1$ convolutional layers; and, finally, after applying normalization on the scores outputted from the convolutional layer by a SoftMax layer, the ore-bearing probability is predicted.

The key technologies used in our lightweight CNNs are as follows:

First, in the characteristic channel depth-increasing part, convolutional layers are used to extract the neighboring spatial characteristics and excavate the dependencies between different ore-controlling factors. Usually, the larger the convolution kernel size, the larger the receptive field, but the larger the amount of computation and parameters. To reduce the number of calculations and parameters while

ensuring that the receptive field is large enough, we replace one $7 \times 7 \times 7$ convolution kernel with three $3 \times 3 \times 3$ convolution kernels and replace one $5 \times 5 \times 5$ kernel with two $3 \times 3 \times 3$ kernels (Table 2). Then, a pooling layer with a size of $3 \times 3 \times 3$ is used to extract the main regional characteristics while removing redundant information, thus preventing the model from over-fitting and improving the generalization ability of the model.

Second, two inception structures are used to increase the richness of the extracted characteristics. To reduce the training time and memory consumption while maintaining training accuracy, traditional deeper networks were not used as usual. Instead, the increased richness of characteristics is extracted at limited depth by increasing the network width. This part is derived from the inception structure of GoogLeNet, which contains four branches. The first branch is a $1 \times 1 \times 1$ convolution layer which performs channel interaction, discovers dependencies between different ore-controlling factors, and extracts potential ore-controlling factors. Meanwhile, the non-linear characteristics are greatly increased in this branch. The second branch comprises a $3 \times 3 \times 3$ max-pooling layer and a $1 \times 1 \times 1$ convolution layer, which acts to determine potential relationships between the main characteristics of the different ore-controlling factors. The third branch consists of a $1 \times 1 \times 1$ convolution layer and a $3 \times 3 \times 3$ convolution layer, while the fourth branch consists of a $1 \times 1 \times 1$ convolution layer and two $3 \times 3 \times 3$ convolution layers. The difference between the third and fourth branches is that the receptive fields to extract the spatial distribution characteristics of neighborhoods differ. Finally, the outputs of the four branches are jointed into the channels to establish a final characteristic map from the inception structure.

Third, a skip connection and deconvolution are utilized to restore the block size. The skip connection can link deep, coarse, and semantic

Table 5

The hyperparameters of the 3D CNN model.

Layer		Kernel Size	Stride	Padding	Output Channel
Characteristic depth deepening	Input	–	–	–	7
	Conv	$3 \times 3 \times 3$	[1, 1, 1]	Same	20
	Conv	$3 \times 3 \times 3$	[1, 1, 1]	Same	32
	Conv	$3 \times 3 \times 3$	[1, 1, 1]	Same	64
	Max Pool	$3 \times 3 \times 3$	[2, 2, 2]	Same	64
	Conv	$3 \times 3 \times 3$	[1, 1, 1]	Same	128
	Conv	$3 \times 3 \times 3$	[1, 1, 1]	Same	192
	Max Pool	$3 \times 3 \times 3$	[2, 2, 2]	Same	192
Characteristic extraction	Branch_1	Conv	$1 \times 1 \times 1$	Same	32
	Branch_2	Max Pool	$3 \times 3 \times 3$	[1, 1, 1]	192
		Conv	$1 \times 1 \times 1$	[1, 1, 1]	32
	Branch_3	Conv	$1 \times 1 \times 1$	[1, 1, 1]	32
		Conv	$3 \times 3 \times 3$	[1, 1, 1]	64
	Branch_4	Conv	$1 \times 1 \times 1$	[1, 1, 1]	32
		Conv	$3 \times 3 \times 3$	[1, 1, 1]	64
		Conv	$3 \times 3 \times 3$	[1, 1, 1]	128
	Connect	–	–	–	256
	Branch_1	Conv	$1 \times 1 \times 1$	[1, 1, 1]	64
	Branch_2	Max Pool	$3 \times 3 \times 3$	[1, 1, 1]	256
		Conv	$1 \times 1 \times 1$	[1, 1, 1]	64
	Branch_3	Conv	$1 \times 1 \times 1$	[1, 1, 1]	64
		Conv	$3 \times 3 \times 3$	[1, 1, 1]	128
	Branch_4	Conv	$1 \times 1 \times 1$	[1, 1, 1]	64
		Conv	$3 \times 3 \times 3$	[1, 1, 1]	128
		Conv	$3 \times 3 \times 3$	[1, 1, 1]	256
	Connect	–	–	–	512
	Average Pool	$3 \times 3 \times 3$	[1, 1, 1]	Same	512
Deconvolution	Transform conv	$3 \times 3 \times 3$	[2, 2, 2]	Same	512
	Skip connection	–	–	–	576
	Transform conv	$3 \times 3 \times 3$	[2, 2, 2]	Same	576
Characteristic reduction	Conv	$3 \times 3 \times 3$	[1, 1, 1]	Same	256
	Conv	$1 \times 1 \times 1$	[1, 1, 1]	Same	128
	Conv	$3 \times 3 \times 3$	[1, 1, 1]	Same	64
	Conv	$1 \times 1 \times 1$	[1, 1, 1]	Same	34
	Conv	$3 \times 3 \times 3$	[1, 1, 1]	Same	16
	Conv	$1 \times 1 \times 1$	[1, 1, 1]	Same	2
SoftMax	SoftMax	–	–	–	2

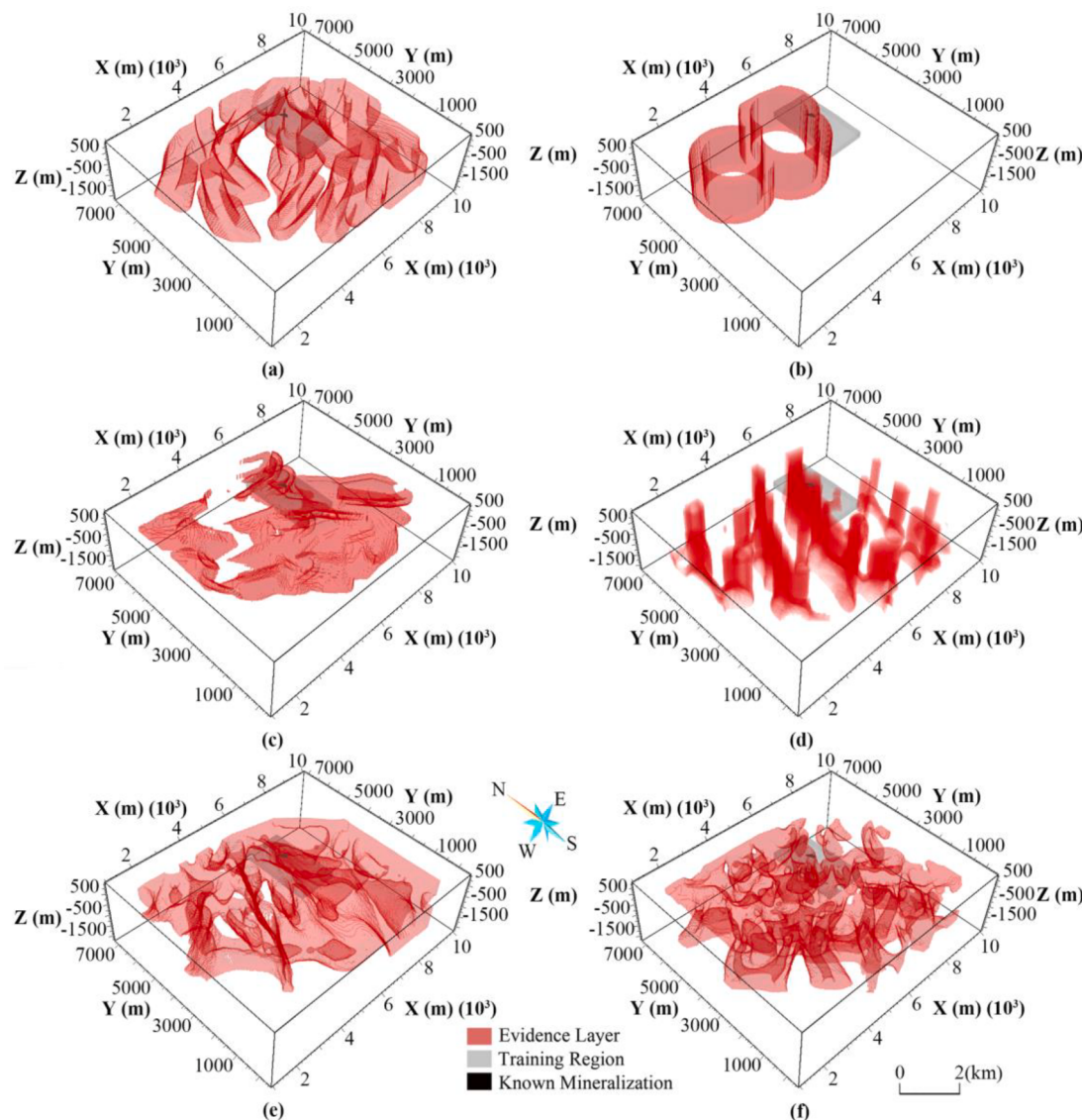


Fig. 10. Spatial distribution of 3D evidence: (a) Distance to fault; (b) distance to paleo-volcanic crater; (c) early Carboniferous granite complex interior distance to the Ganhe Formation; (d) residual gravitational density; (e) magnetic anomaly; and (f) apparent resistivity distribution.

Table 6
Weights (W^+ and W^-) and contrast (C) values for the six available evidences.

Evidence	Prediction variable	W^+	W^-	C
Early Carboniferous granite complex interior distance to the Ganhe Formation	219–425 m	1.28250	-4.80886	6.09136
Distance to fault	$\leq 300 \text{ m}$	0.25882	-4.93502	5.19384
Distance to paleo-volcanic crater	900–1300 m	1.28141	-6.17006	7.45147
Apparent resistivity	0.986–1.94 $\Omega\cdot\text{m}$	0.35831	-1.86196	2.22027
Magnetic anomaly	-0.120–0.060 nT	0.22362	-2.70530	2.92892
Residual gravitational density	7.6×10^{-6} –3.81 $\times 10^{-5} \text{ g/cm}^3$	0.68091	-4.66549	5.34640

characteristics with shallow, fine, and appearance characteristics. By combining coarse and fine characteristics, the model may generate local predictions regarding global structure. We use a 3D deconvolution layer to replace the fully connected layer, in order to achieve end-to-end

learning. Deconvolution can greatly reduce the number of parameters and improve the learning efficiency while implementing end-to-end learning. Using a deconvolution layer not only allows us to output the prediction results for any voxels of a block, but is also more efficient than patch-wise training. Moreover, multiple convolution layers are used to fuse the characteristics of each voxel and reduce the number of characteristic channels. The characteristic channels of the output are same as the number of classification categories. Table 3 shows the number of parameters generated in the two parts of deconvolution and characteristic reduction in Fig. 9. As the fully connected (FC) layer can only be used for patch-wise training, the deconvolution and characteristic reduction parts replace three fully connected layers for parameter calculation. Tables 3 and 4 show the number of parameters for end-to-end learning with deconvolution layers or fully connected layers, respectively. The design of the fully connected layer refers to mature networks, such as VGG-16 (Simonyan and Zisserman, 2015) and AlexNet (Krizhevsky et al., 2017), which use 4096 neurons. The comparison results show that our method effectively reduces the number of parameters used.

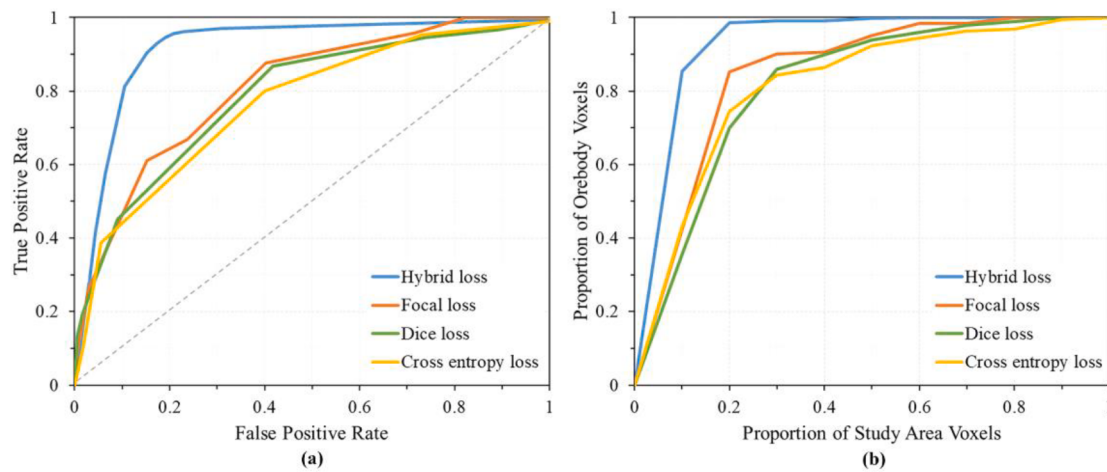


Fig. 11. (a) ROC curves; and (b) ore-controlling rate curves of hybrid loss, focal loss, dice loss, and cross entropy loss.

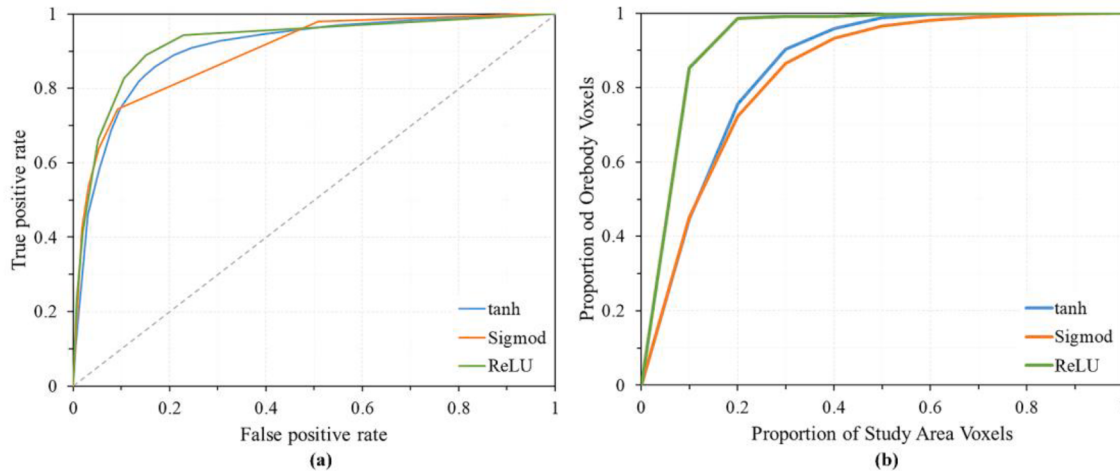


Fig. 12. (a) ROC curves; and (b) ore-controlling rate curves of tanh, Sigmoid, and ReLU.

3.2.2. Optimization

1) A rectified linear unit (ReLU) is added after each convolution operation to prevent gradient vanishing, increase network sparsity, and alleviate over-fitting problems. As the ReLU activation function (Glorot et al., 2011) is non-saturated and non-linear, it can effectively solve the problem of gradient disappearance during back-propagation of the sigmoid function. Meanwhile, ReLU not only can significantly reduce the calculated amount of the whole process, as well as allocate some neuron outputs as 0 to increase network sparsity, decrease parameter interdependence, and alleviate overfitting. A ReLU non-linear map is usually used in convolution layer as its activation function, as follows:

$$f(x) = \max(0, x). \quad (1)$$

2) To mitigate over-fitting, batch normalization (BN) (Sergey and Christian, 2015) is introduced after each convolution operation and activation function. The eigenvalue distribution of each layer will increasingly approach the top and bottom bounds of the activation function's output interval (i.e., the saturation interval of the activation function) when the network depth increasing, resulting in vanishing of the gradient. By regressing the eigenvalue distribution of the layer back to the standard normal distribution, the gradient

becomes larger, which can prevent gradient vanishing and accelerate the rate of convergence.

3) To improve the sensitivity of the network to minority classes, a hybrid loss function is employed. The proportion of ore voxels in the training area is very small, with most of the voxels belonging to the non-ore class. In this case, if the same weight is given to the ore and non-ore samples in the loss function, the model training will be biased towards the class with larger proportion, which results in becoming stuck in local optima and decreased prediction accuracy of the model. Therefore, to deal with class imbalance, a hybrid loss that combines dice loss (Li et al., 2020) and focal loss (Lin et al., 2017) is used to improve the sensitivity of the network to ore class.

The L_{Dice} value is only related to the similarity between the true and predicted result, and is not related to the number of training samples. Thus, dice loss may experience drastic gradient changes during model training, resulting in unstable model training.

$$L_{Dice} = 1 - \frac{1}{N} \left(\frac{2 \sum_{n=1}^N y_n y'_n + o}{\sum_{n=1}^N y_n + \sum_{n=1}^N y'_n + o} + \frac{2 \sum_{n=1}^N (1 - y_n)(1 - y'_n) + o}{\sum_{n=1}^N (1 - y_n) + \sum_{n=1}^N (1 - y'_n) + o} \right), \quad (2)$$

where L_{Dice} is the dice loss, N is the total number of the voxels in a block, y_n is the true ore class, y'_n is the predicted probability for the ore class, and o is a constant term, which is added to avoid a denominator with

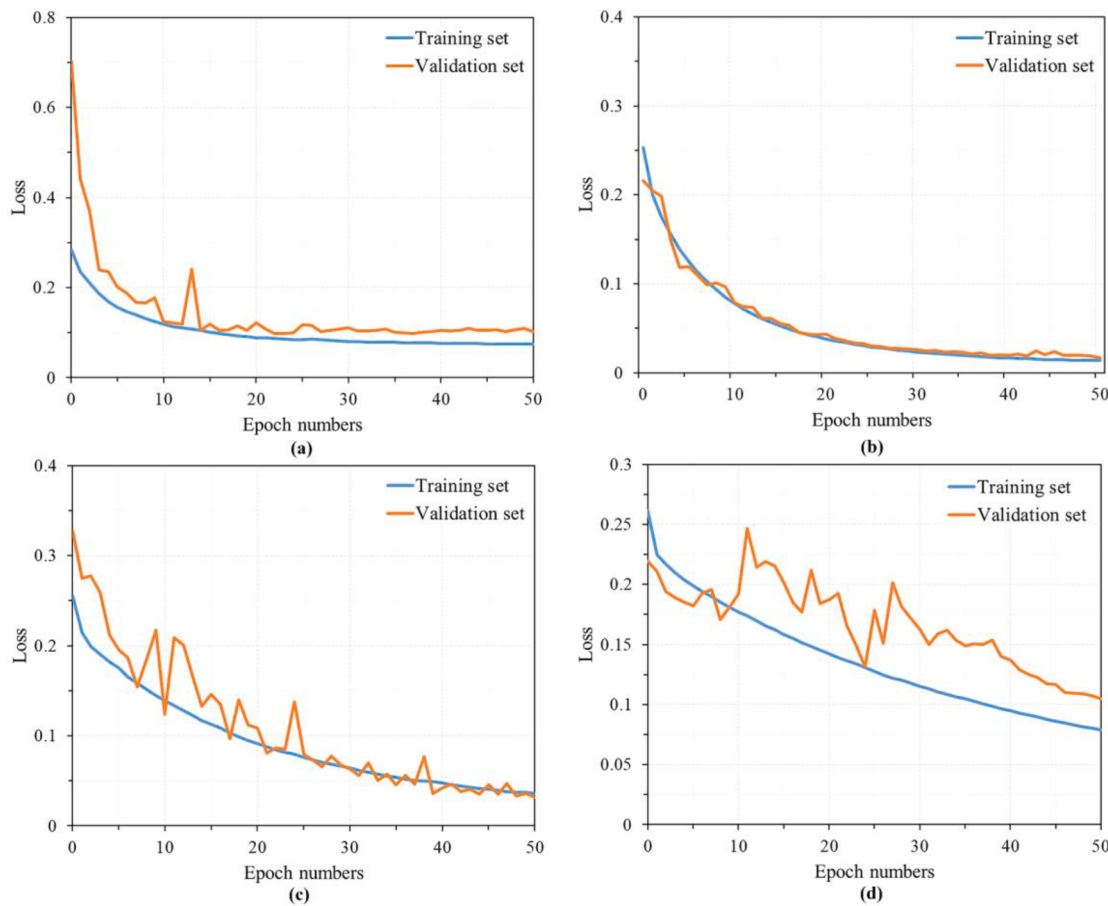


Fig. 13. Loss with the learning rate of (a) 0.01; (b) 0.005; (c) 0.002; and (d) 0.001.

value of zero in the equation.

The focal loss is modified based on the standard cross-entropy loss by increasing α and γ to reduce the weight of negative samples, which is convenient for sample classification. If the number of negative samples is too large, it will have high weight in the loss, and most are easy to classify, such that the optimization of the model will deviate from what we want. The coefficient α is introduced to control the weights of positive and negative samples in the total loss, while the focus parameter γ is used to reduce the weight to classify the samples.

$$L_{Focal} = -\alpha_n (1 - y'_n)^\gamma, \quad (3)$$

where L_{Focal} is the focal loss, α_n is the coefficient for balancing ore and non-ore classes, and γ is a tunable focusing parameter.

In this study, the hybrid loss function is designed to remain stable and avoid local optima:

$$L_{Hybrid} = L_{Dice} + L_{Focal}. \quad (4)$$

3.2.3. Parameter configuration

The hyperparameter settings for the 3D CNN model used in this study are shown in Table 5. Here, each convolutional layer is processed by the ReLU activation function and the BN layer. The value of the learning rate is 0.005.

3.3. Three-dimensional WofE model

The WofE model, based on Bayesian theorem, utilizes conditional probabilities to generate the posterior probability of the mineralization (Agterberg, 1991). The WofE computing is based on concept of prior, conditional, and posterior probabilities. If the study area (corresponding

to each factor) is divided into T voxels, with D voxels including known ore bodies, the prior probability $P(D)$ is expressed as

$$P(D) = N(D)/N(T) \quad (5)$$

The odds ratio of $P(D)$ is expressed as

$$O(D) = \frac{P(D)}{1 - P(D)}. \quad (6)$$

The WofE approach often employs a pair of weights calculated in log-linear variant of the Bayesian probability to weight the relevance of evidence (Zhang et al., 2015). The positive weight (W^+) and negative weight (W^-) indicate the existence of the evidence B and its absence \bar{B} , respectively.

$$W = \begin{cases} W^+ = \ln \frac{P(B/D)}{P(\bar{B}/D)} = \ln \frac{N(B \cap D)/N(D)}{N(\bar{B} \cap D)/N(D)} \\ W^- = \ln \frac{P(\bar{B}/D)}{P(B/\bar{D})} = \ln \frac{N(\bar{B} \cap D)/N(D)}{N(B \cap \bar{D})/N(D)} \\ 0 \end{cases} \quad (7)$$

The W^+ and W^- reflect the characteristics of the cross-correlation between the known training voxels and the evidence layer B . If a voxel has no data, then its weight is set as 0. The weights are calculated for each evidence layer. Then, the posterior probability odds of every voxel is calculated as:

$$\ln(O_{posterior}) = \ln(O(D)) + \sum_{i=1}^n w_i^k (i = 1, 2, 3, \dots, n). \quad (8)$$

The posterior probability is a key index to depict the mineralization potential of an area, which represents the metallogenic favorability of

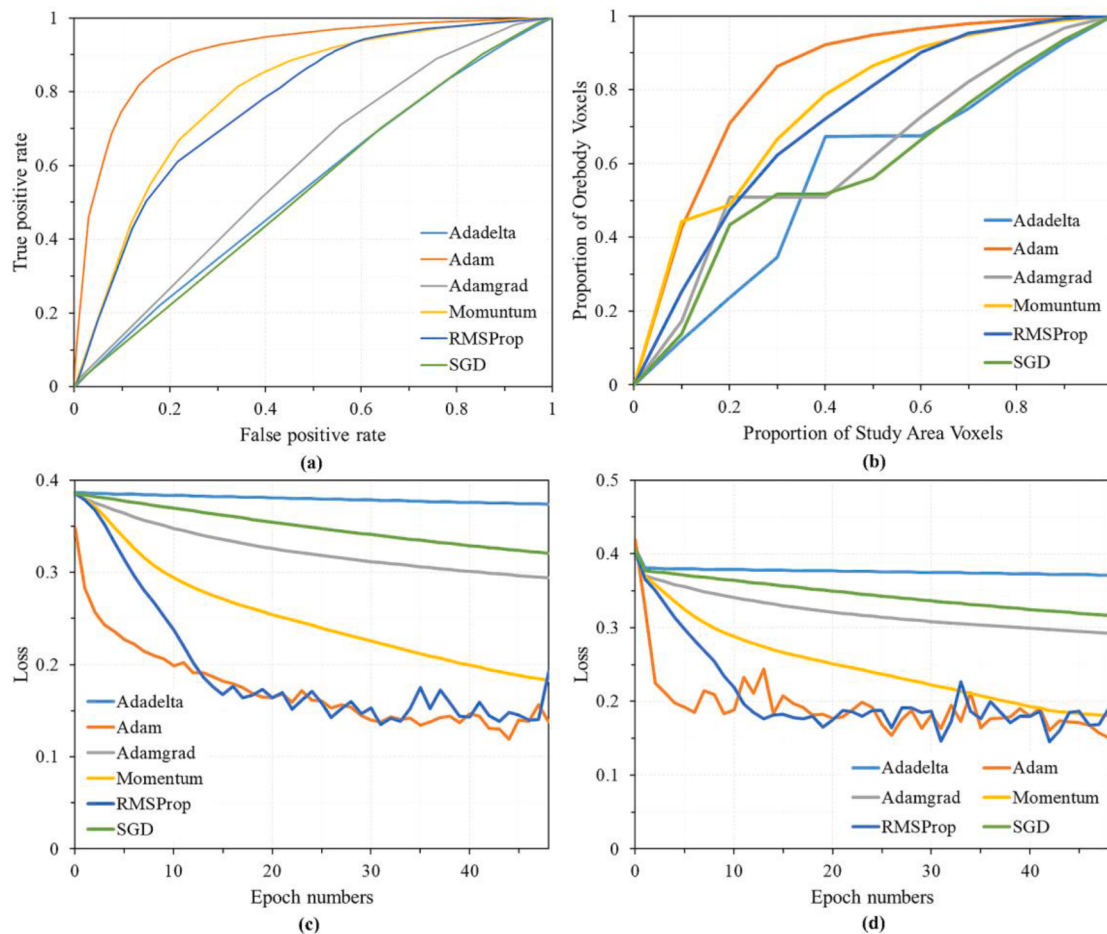


Fig. 14. (a) ROC curves; (b) ore-controlling rate curves; (c) training loss; and (d) testing loss of Adadelta, Adam, Adamgrad, Momentum, RMSProp, and SGD.

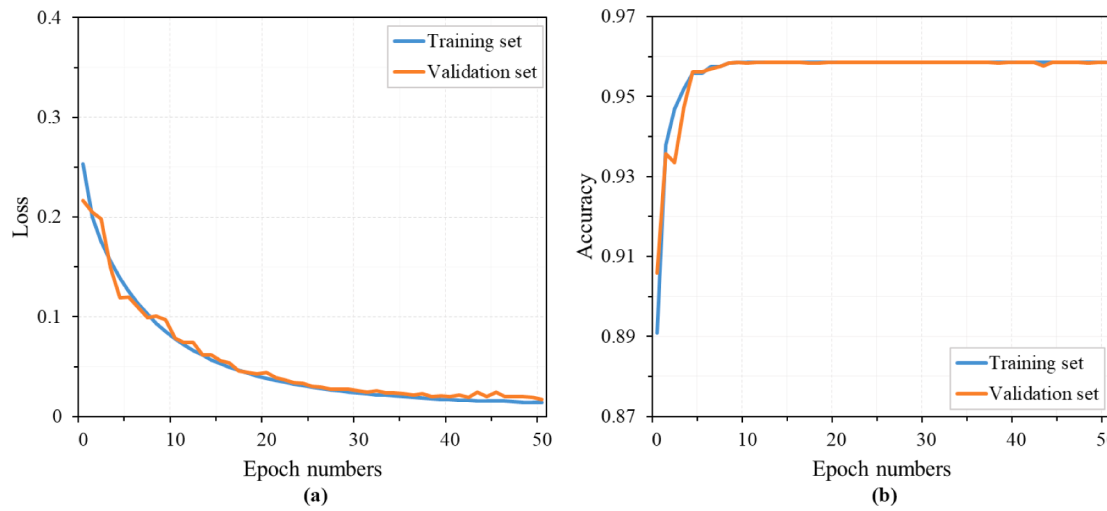


Fig. 15. The training process for CNN modeling: (a) Hybrid loss; and (b) accuracy in different epochs.

each voxel as:

$$P_{\text{posterior}} = \frac{O_{\text{posterior}}}{1 + O_{\text{posterior}}} \quad (9)$$

Data pre-processing in the WofE method comprises three stages: 1) Defining the favorable ore-controlling characteristics, according to the distribution of mineralization; 2) combining knowledge- and data-driven methods to determine the thresholds values for B and

\bar{B} of the evidence; and 3) building the binary evidence, in which the favorable metallogenic areas are assigned a value of 1, while the other areas are assigned a value of 0 (Deng, 2009). The difference between the positive and negative weights, known as the contrast C , is calculated as

$$C = W^+ - W^- \quad (10)$$

The contrast, which combines the impacts of the two weights, provides an overall estimation of spatial cross-correlation between the

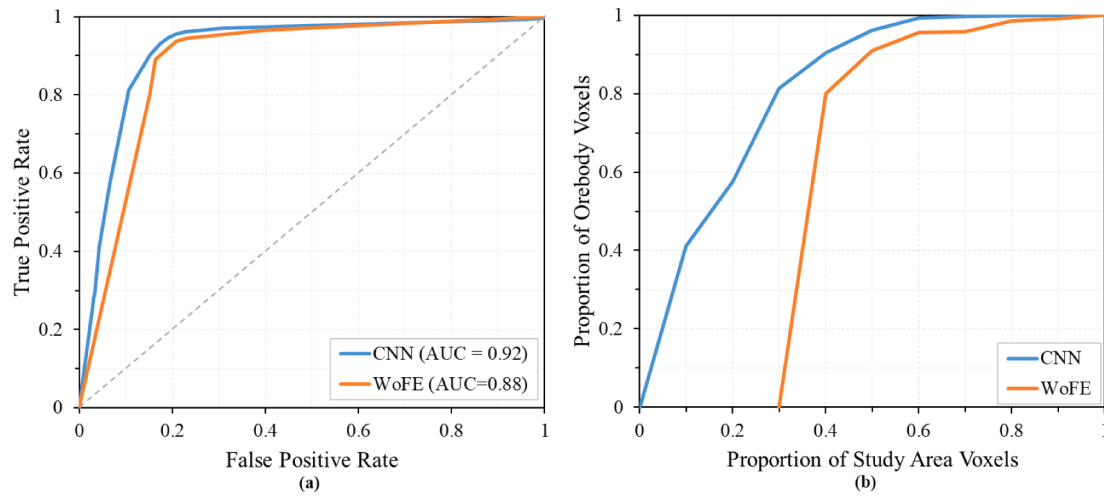


Fig. 16. (a) ROC curves; and (b) ore-controlling rate curves of CNN and WoFE models.

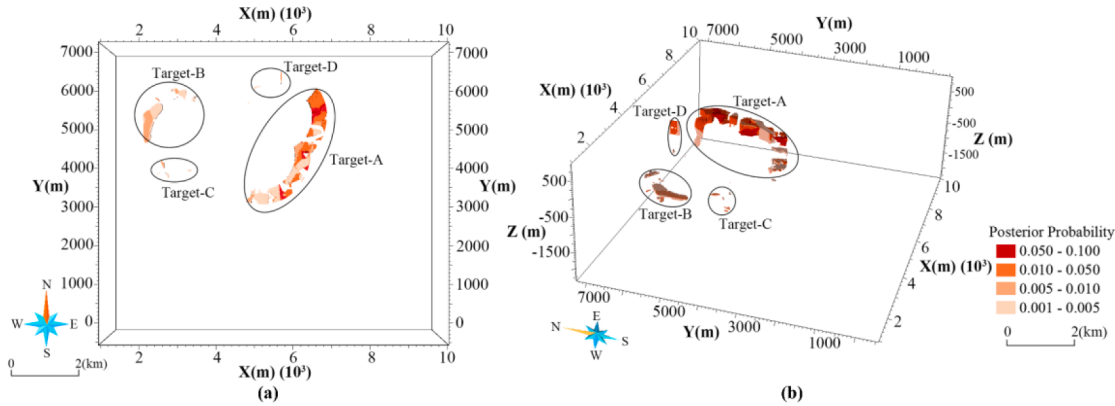


Fig. 17. The posterior probabilities of the 3D MPM by the WoFE method: (a) Top view of target areas; and (b) side view of target areas.

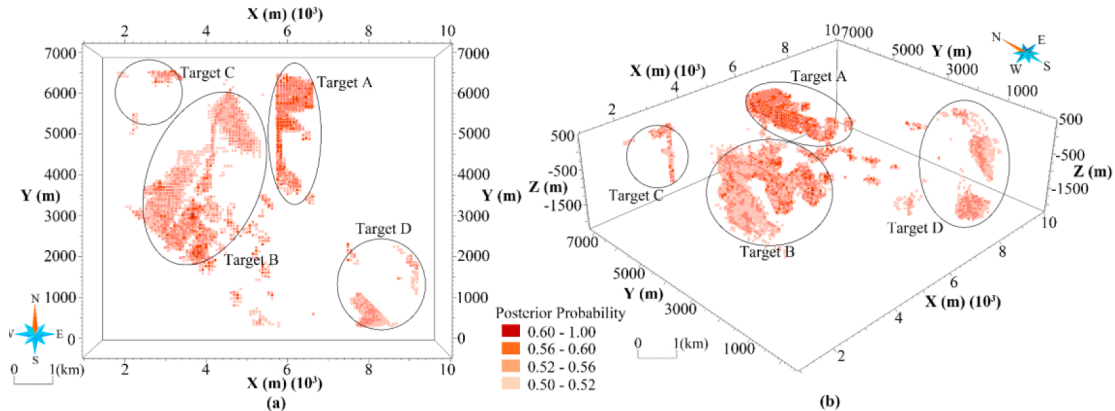


Fig. 18. The posterior probabilities of the 3D MPM by the proposed CNN method: (a) Top view of target areas; and (b) side view of target areas.

mineralization *D* and the evidence layer *B*. For a positive cross-correlation, *C* is always positive, whereas *C* is negative when negative spatial cross-correlation presents.

4. Results and discussions

4.1. WoFE modeling

Following statistical analysis of all ore-controlling factors, a total of

six predictors were chosen to serve as the 3D evidence layers. The model of the study area was composed of 769 million voxels with an individual size of 5 m × 5 m × 5 m. Every voxel was assigned with the property of mineralization prospecting. The continuous data were reclassified into discrete classes. The thresholds for binary reclassification were determined by the spatial cross-correlation between the known mineral occurrence pattern and the derived multiple evidential layers. Only 3D evidence layers exhibiting the strong values of weights were retained as shown in Fig. 10, which are characterized by significant confidence.

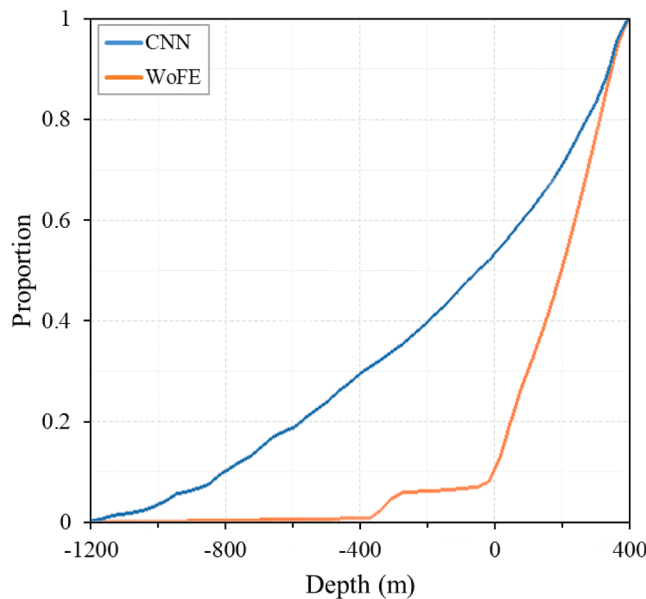


Fig. 19. Depth distribution of prediction results.

Table 6 provides the weight and contrast values for these 3D evidence layers.

4.2. CNN modeling

We implemented the 3D CNN model using the TensorFlow framework (Abadi et al., 2016). To capture the potential correlations between characteristics, we retained the continuity of input features to the greatest extent possible within our CNN method. Consequently, the fundamental inputs for the CNN model comprised six continuous ore-controlling factors, as shown in Fig. 7. To avoid the biased CNN prediction results caused by the large difference of magnitude order among the data, the continuous data were normalized into the interval [0, 1] by max–min normalization, and the label were processed by one-hot encoding. In the training area, 7278 positive ore voxels and 1,627,362 negative non-ore voxels in all 3D-block samples of size $16 \times 16 \times 16$ voxels were extracted from the entire model and stored, with a voxel size of $5\text{ m} \times 5\text{ m} \times 5\text{ m}$. These 3D blocks, with 50 % inter-overlap ratio in all three coordinate axes, formed the training set. To balance the ore-bearing and non-ore-bearing categories, non-ore-bearing blocks were sampled in the range of 200 m to 600 m far away from the known ore bodies in the prospecting area. Then, 80 % and 20 % of the data with label were used for training and testing, respectively. Six ore-controlling factors were used as inputs to the 3D CNN model, with one of them occupying two channels while the other five factors occupied the remaining five channels, respectively. We adopted five-fold cross-validation to prevent the unreasonable division of the training and testing sets from affecting the model training. Our training process effectively batched the whole study area into overlapping blocks composed of regular voxels, instead of randomly sampling blocks over a full data set, resulting in higher variance batches to accelerate the convergence. Gradient computation is driven by the training distribution in stochastic optimization. Therefore, our approach is more efficient than random block sampling, reducing the unnecessary batch number.

To decrease the impact of class imbalances between ore-bearing and non-ore-bearing samples, the hybrid loss was introduced. Fig. 11 shows the receiver operating characteristic (ROC) and the ore-controlling rate curves of CNN models trained with hybrid loss, focal loss, dice loss, and cross entropy loss. The ROC curve is usually evaluated by the area under the curve (AUC) which varies between 0.5 and 1. In our case, a higher AUC indicates a more efficient prospectivity model. In this study, the

ROC curves were plotted according to the blocks in the testing set. The process of plotting ore-controlling rate curves includes statistically calculating all blocks in the whole study area. The predicted ore-bearing posterior probability of all voxels were first sorted in descending order. Subsequently, the retrieved probabilities were then reclassified using different thresholds. Finally, we calculated the success rate via counting the number of known voxels for segmentation. Both the ROC and the ore-controlling rate curves of our CNN model using the hybrid loss excel other loss functions, which demonstrates that hybrid loss effectively enhanced the focus on the ore-bearing samples in CNN training.

The role of the activation function is to introduce non-linearity into the CNNs, and the performance of the CNN model is usually influenced by the choice of activation function. Fig. 12 shows the ROC and the ore-controlling rate curves of our CNN models trained with tanh, Sigmoid, and ReLU, which demonstrates that ReLU can effectively enhance the mining of non-linearity information in CNN training.

To determine the optimal learning rate, convergence rates were tested at learning rates of 0.01, 0.005, 0.002, and 0.001, respectively (Fig. 13). With the same epoch number, loss curves of learning rates of 0.002 and 0.001 converge slowly and tend to fall into local optima, while loss curve of learning rate of 0.01 converges too quickly and tends to miss the global optimum. Therefore, the final learning rate was set to 0.005.

Fig. 14 shows the performances of CNN models trained with Adadelta (Zeiler, 2012), Adam (Kingma and Ba, 2015), Adamgrad (Duchi et al., 2011), Momentum (Polyak, 1964), RMSProp (Tieleman and Hinton, 2012), and SGD (Ruder, 2016) optimizers. Both the ROC and the ore-controlling rate curves of the CNN models using the Adam excel other five optimizers. Meanwhile, both the training loss and testing loss curves of CNN model with the Adam optimizer converge quickly.

In the CNN training process, 50 epochs were required to achieve full convergence, spending about 1 h on one Nvidia GeForce RTX 2060 Super 8 GB graphics card. Fig. 15 demonstrates the performances on the training and testing sets. The both testing accuracy (loss) gradually rose (decreased) in the training process. When the convergence was reached, the training and testing loss values remained around 0.014 and 0.016, respectively. Finally, the training accuracy and the testing accuracy reached to 0.959 and 0.958, respectively. In general, the results demonstrated the proposed CNN trainable to recognize the correlation to mineralization.

While the training runtime and evaluation metrics for a standard 3D CNN model are all deemed acceptable and comparable in the parallel computing environment, our proposed light 3D CNN with end-to-end learning consumes less time, especially when predicting a vast number of voxels in unknown areas, through pixel-wise processing, saving thousands of times the computational effort.

4.3. Model performances

We plotted the receiver operating characteristic (ROC) and ore-controlling rate curves (Fig. 16). Fig. 16a demonstrates the ROC curves of the CNN and WofE approaches for 3D MPM. The ROC curve of the proposed CNN approach for 3D MPM, with an AUC value of 0.92, can be seen to be significantly steeper towards the upper left corner than that of the WofE approach, with an AUC value of 0.88. Overall, the CNN approach outperformed the WofE approach in 3D MPM and better identified both classes (i.e., ore-bearing and non-ore-bearing voxels). Fig. 16b indicates that the top 30 % of voxels based on the CNN method contained 80 % of the known ore-bearing voxels, while the first 40 % of the voxels of the WofE method achieved this ratio. The top 70 % voxels of the CNN method contained 100 % of the known ore-bearing voxels, while the WofE method achieved only about 98 % of the known ore-bearing voxels under this threshold. Furthermore, the result of the WofE model included all known ore-bearing voxels only when raising the threshold to 95 %. These comparisons imply that the proposed CNN method has greater localization efficiency in recognizing high

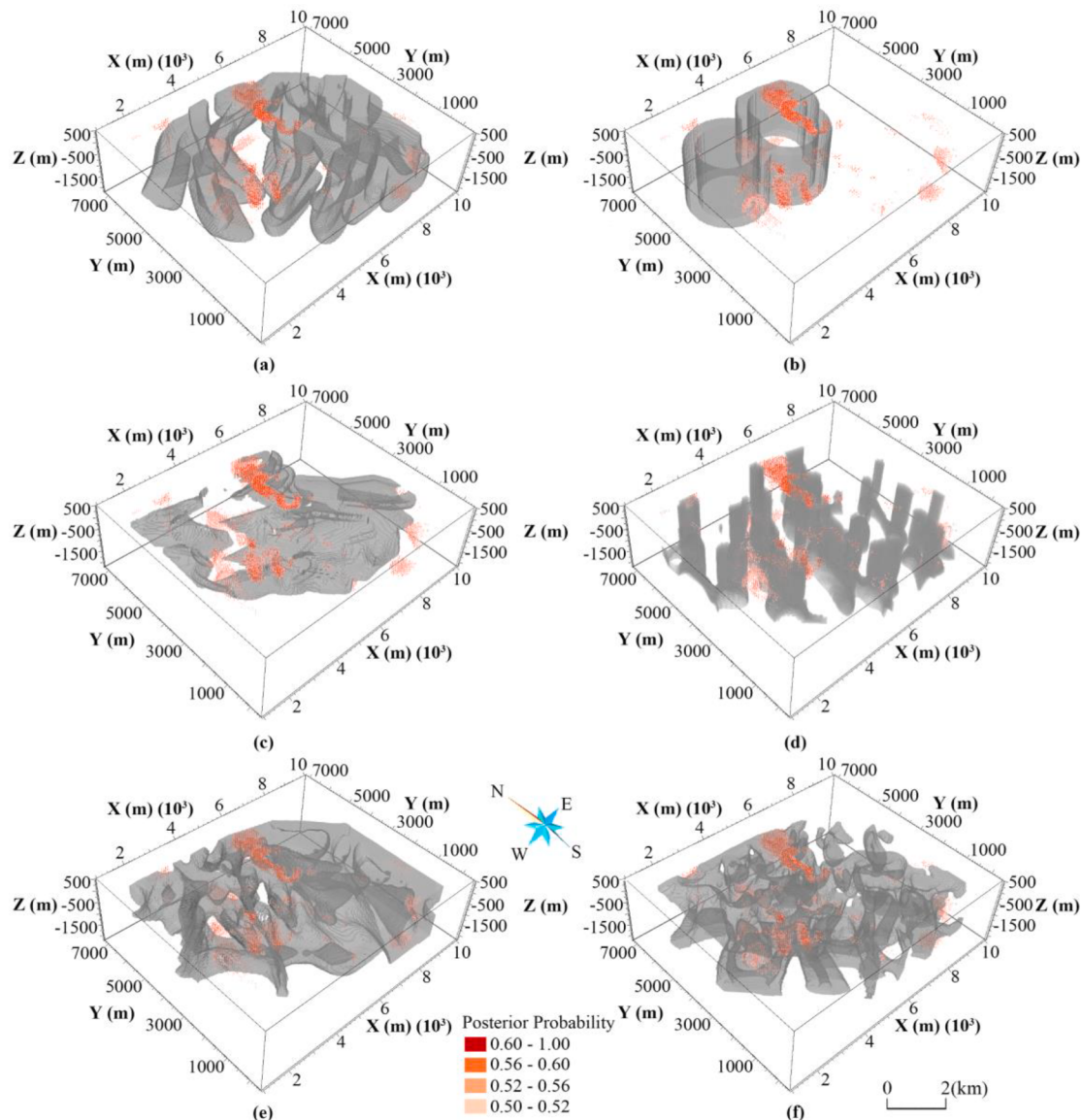


Fig. 20. CNN prediction results overlaid with evidence factors: (a) Distance to fault; (b) distance to paleo-volcanic crater; (c) early Carboniferous granite complex interior distance to Ganhe Formation; (d) residual gravitational density; (e) magnetic anomaly; and (f) apparent resistivity distribution.

favorability areas.

The potential mineral prospecting areas with high-favorability were selected for future exploration. The high-favorability regions were distinguished from the low-favorability background through an optimal threshold maximum determined by the Youden index (MYI) (Ruopp et al., 2008). The MYI obtained from the ROC curve was adopted to evaluate the optimal probability thresholds for WofE and CNN as 0.50 and 0.001, respectively. Figs. 17 and 18 show the high-favorability targets resulting from the CNN and WofE models, respectively. According to the prediction results, each model identified four mineral exploration targets. The favorability values obtained by the WofE were all less than 0.1. The two targets A and B were relatively large and located in high-favorability targets, which could be considered as potential metallogenic areas. However, targets C and D were relatively small and had low favorability values, making them of low significance for mineral prospecting. Compared with WofE, the targets from the CNN basically covered the targets obtained by WofE. In general, the targets from the CNN were mainly distributed at depths of ~200 m to ~500 m (Fig. 19). The high favorability areas were mainly distributed in targets A and B; however, again, the favorability values of targets C and D were

relatively low. Generally, high-favorability areas were mainly concentrated in the northwest of the study area, while low-favorability areas were scattered in the southeast. As the calculation process of WofE modeling is a simple linear calculation regarding the binarized evidence layer, it failed to exploit the complex metallogenic characteristics. However, the CNN method better learned the potential ore-controlling characteristics through the non-linear calculation process, and could easily describe the potential relationships between different characteristics. Therefore, this method has advantages in predicting deep unknown ore-bearing areas.

4.4. Prospecting targets

Figs. 20 and 21 show the prospecting targets of CNN and WofE overlaid on the evidence factors, respectively. The prediction results of the CNN can be seen to basically cover those of the WofE. The prospecting targets of the CNN were mainly enriched in the NE-trending fault distance field from 0 to 400 m, the paleo-volcano crater distance field from 0 to 2200 m, the granite complex interior distance field from 0 to 700 m, near the transition zone between high and low gravitational

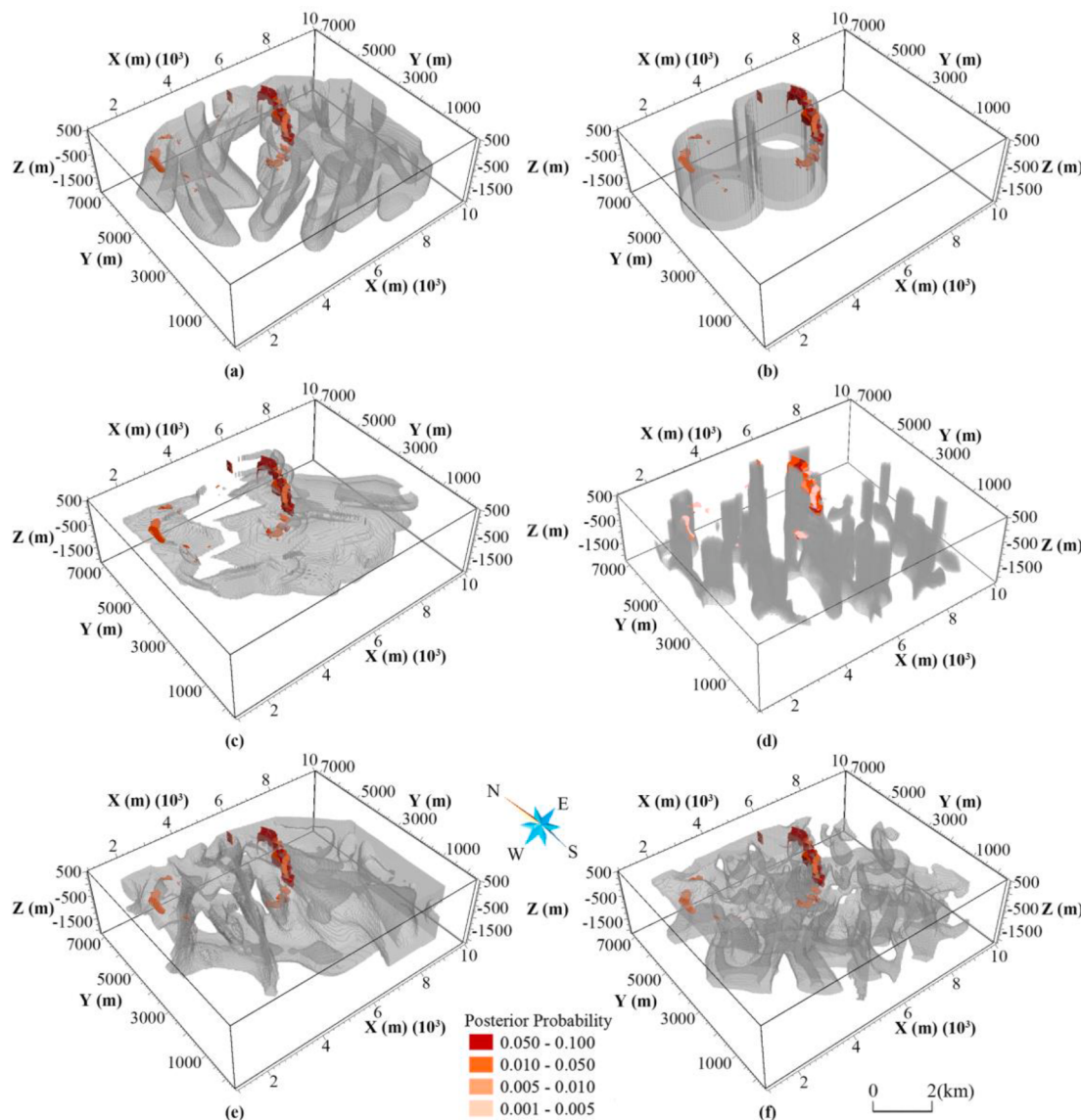


Fig. 21. WofE prediction results overlaid with evidence factors: (a) Distance to fault; (b) distance to paleo-volcanic crater; (c) early Carboniferous granite complex interior distance to Ganhe Formation; (d) residual gravitational density; (e) magnetic anomaly; and (f) apparent resistivity distribution.

density, near the negative magnetic anomaly, and near the transition zone between high and low resistivity anomalies, which fit well with the known geophysical prospecting indicators. The CNN presented a strong ability to automatically identify favorable metallogenic conditions. For the WofE, the prospecting targets mainly have common parts in the six evidence factors, and their locations were greatly affected by the paleo-volcano crater distance field. Therefore, the prediction results of WofE method were greatly affected by the selection of evidence factors and the binarizing threshold of the evidence factors, which are greatly affected by the expert experience. For classification problems with a very small number of positive samples in this study, the CNN method has more advantages, in terms of sensitivity to the few-sample categories and better recognition ability, which is more credible than using expert experience to adjust the evidence factors in the WofE.

The 3D MPM process of the WofE approach had the following problems: 1) It only pays attention to extracting quantitative anomalies, while neglecting the significance of the spatial auto-correlation of each factor and the cross-correlation between different factors; 2) the metallogenic process has strong stochasticity and non-linearity, but the prediction process of WofE is a linear transform, making it unable to portray the non-linear relationship between mineralization and factors

well; and 3) the ore-controlling factors are transformed to binary variables by experience, which only takes advantage of main ore-controlling information while ignoring others.

According to the available data, there were a total of 769 million voxels in the entire study area, while only 7278 voxels are known to be ore-bearing. Therefore, the WofE strategy of generating evidence factors is likely to ignore some favorable metallogenic conditions, which was also confirmed from the main target area being located in and near the training area. However, the CNN strategy involves automatically learning the ore-controlling factors related to mineralization by taking the original continuous characteristics as input. Therefore, the CNN can greatly reduce the uncertainty brought by expert experience, and its non-linear simulation process is more efficient in terms of utilizing characteristics.

Compared with the traditional 3D MPM of WofE, the CNN-based 3D MPM method uses a deep network architecture to capture the correlations between different ore-controlling factors and mineralization. In addition, the powerful representation learning capability of the CNN realizes the automatic mining of potential ore-controlling factors, providing a novel means to avoid the tedious work of designing predictor variables, as in traditional MPM approaches. Moreover, this

method learns directly from the 3D geological model, which makes it faithful to the massive training set to provide more objective results, as well as preventing the limitations of subjective understanding and shortage of prior knowledge. Therefore, the CNN-based 3D MPM approach could significantly minimize effort and prospecting risks when predicting concealed ore bodies.

5. Conclusion

In this study, we proposed a lightweight 3D CNN model for MPM using the GoogleNet inception structure combined with deconvolution to achieve end-to-end learning, which is more efficient and requires fewer parameters than traditional CNN methods. As demonstrated in the case study of a structure-controlled hydrothermal gold deposit in the Sanhetun area of Heilongjiang Province, NE China, the proposed CNN approach for 3D MPM presents several advantages over the method of WoFE:

- 1) Due to the representation learning capability of CNNs, the proposed CNN approach for 3D MPM can perform characteristic learning easily from 3D geological models and automatically encapsulate the complex correlations between multivariate characteristics for MPM, improving 3D MPM recognition accuracy and prediction efficiency.
- 2) The CNN approach for 3D MPM eliminates the need for extensive preprocessing of ore-controlling factors and effectively learns informative representations of prospectivity, alleviating the complexity associated with predictor design in MPM.
- 3) The utilization of GoogleNet's inception unit for multi-channel characteristic extraction delves deep into feature extraction, combining shallow and deep characteristics via skip connections to prevent convergence on local optima. This significantly reduces the estimated parameters in the training process compared to traditional complex CNN networks. Additionally, the proposed end-to-end method, predicting the class of each voxel in a 3D block, and achieving per-pixel losses back-propagation through deconvolution, proves to be highly efficient even with massive dataset. The deconvolution layer, replacing the fully connected layer, avoids the estimation of a large number of parameters and enhances prediction accuracy. Pixel-wise learning for end-to-end training substantially enhances training efficiency and accuracy, producing appropriately sized output with efficiently handling extensive datasets.
- 4) The proposed CNN approach for 3D MPM avoids the constraints of empirical knowledge and excellent metallogenic conceptual models by learning the ore-controlling characteristics from the spatial patterns of 3D geological models. This yields more objective results and greater faithfulness to the massive training set, which in turn provides deeper insights into prospecting targets.

For these reasons, the suggested method offers an innovative and potent tool for reducing the workload and exploration risks associated with concealed orebody prospecting.

However, there are several limitations. Our network architecture shows good performance in the Sanhetun area, however, whether it is universally applicable to other areas requires further validation. Furthermore, the explaining of the CNN approach is another concern, which opens the CNN black box, which will hopefully drive the MPM more understandable. In the future, more exploration engineering is needed to verify the validation of predicted results as well as the generalizability of the model. It is also needed to find ways to visualize the internal workings of CNNs and enhance their interpretability in MPM.

Declaration of competing interest

The authors declare that they have no known competing financial interests or personal relationships that could have appeared to influence

the work reported in this paper.

Data availability

Data will be made available on request.

Acknowledgements

This study was supported by grants from the National Natural Science Foundation of China (Grant No. 42072326) and China Geological Survey Work Project (Grant No. DD20190156). The authors thank Dr. ZHANG Chun-peng, Dr. LIU Bao-shan (Shenyang Center of China Geological Survey), and Dr. LIU Wen-yu (East China University of Technology) for their kind assistance with data collection. We also thank the MapGIS Laboratory Co-Constructed by the National Engineering Research Center for Geographic Information System of China and Central South University for providing MapGIS® software (Wuhan Zondy Cyber-Tech Co. Ltd., Wuhan, China).

References

- Abadi M, Barham P, Chen J, Chen Z, Davis A, Dean J, Devin M, Ghemawat S, Irving G, Isard M, Kudlur M, Levenberg J, Monga R, Moore S, Derek B, Tucker P, Vasudevan V, Warden P, Wicke M, Yu Y, Zheng X. 2016. TensorFlow: A system for large-scale machine learning[J]. In 12th Advanced Computing Systems Organization symposium on operating systems design and implementation ({OSDI} 16): 265–283.
- Agterberg, F.P., 1991. Combining indicator patterns in weights of evidence modeling for resource evaluation[J]. Nonrenewable Resources 1 (1), 35–50.
- Ali, A.M., Radwan, A.E., Abd El-Gawad, E.A., Abdel-Latif, A.-S.-A., 2021. 3D Integrated Structural, Facies and Petrophysical Static Modeling Approach for Complex Sandstone Reservoirs: A Case Study from the Coniacian-Santonian Matulla Formation, July Oilfield, Gulf of Suez, Egypt[J]. Nat. Resour. Res. 31 (1), 385–413. <https://doi.org/10.1007/s11053-021-09980-9>.
- Ao, Z., Sun, Y., Pan, X., Xin, Q., 2022. Deep Learning-Based Spatiotemporal Data Fusion Using a Patch-to-Pixel Mapping Strategy and Model Comparisons[J]. IEEE Trans. Geosci. Remote Sens. 60, 1–18. <https://doi.org/10.1109/tgrs.2022.3154406>.
- Basson, I.J., Anthonissen, C.J., McCall, M.J., Stoch, B., Britz, J., Deacon, J., Strydom, M., Cloete, E., Botha, J., Bester, M., Nel, D., 2017. Ore-structure relationships at Sishen Mine, Northern Cape, Republic of South Africa, based on fully-constrained implicit 3D modelling[J]. Ore Geol. Rev. 86, 825–838. <https://doi.org/10.1016/j.oregeorev.2017.04.007>.
- Bérubé, C.L., Olivo, G.R., Chouteau, M., Perrotout, S., Shamsipour, P., Enkin, R.J., Morris, W.A., Feltrin, L., Thiémonge, R., 2018. Predicting rock type and detecting hydrothermal alteration using machine learning and petrophysical properties of the Canadian Malartic ore and host rocks, Pontiac Subprovince, Québec, Canada[J]. Ore Geol. Rev. 96, 130–145. <https://doi.org/10.1016/j.oregeorev.2018.04.011>.
- Cirean, D.C., Giusti, A., Gambardella, L.M., Schmidhuber, 2012. Deep Neural Networks Segment Neuronal Membranes in Electron Microscopy Images[J]. Adv. Neural Inf. Proces. Syst. 25, 2852–2860.
- de la Varga, M., Schaaf, A., Wellmann, F., 2019. GemPy 1.0: open-source stochastic geological modeling and inversion[J]. Geosci. Model Dev. 12 (1), 1–32. <https://doi.org/10.5194/gmd-12-1-2019>.
- Deng, M., 2009. A Conditional Dependence Adjusted Weights of Evidence Model[J]. Nat. Resour. Res. 18 (4), 249–258. <https://doi.org/10.1007/s11053-009-9101-5>.
- Deng, K., Li, Q., Chen, Y., Zhang, C., Zhu, X., Xu, Q., 2018. Geochronology, geochemistry and Sr-Nd-Pb-Hf isotopes of the Early Jurassic granodiorite from the Sankuangou intrusion, Heilongjiang Province, Northeastern China: Petrogenesis and geodynamic implications[J]. Lithos 296–299, 113–128. <https://doi.org/10.1016/j.lithos.2017.10.016>.
- Deng, H., Zheng, Y., Chen, J., Yu, S., Xiao, K., Mao, X., 2022. Learning 3D mineral prospectivity from 3D geological models using convolutional neural networks: Application to a structure-controlled hydrothermal gold deposit[J]. Comput. Geosci. 161 <https://doi.org/10.1016/j.cageo.2022.105074>.
- Duchi, J., Hazan, E., Singer, Y., 2011. Adaptive Subgradient Methods for Online Learning and Stochastic Optimization[J]. J. Mach. Learn. Res. 12 (null), 2121–2159.
- Farahbakhsh, E., Hezarkhani, A., Eslamkish, T., Bahroudi, A., Chandra, R., 2020. Three-dimensional weights of evidence modelling of a deep-seated porphyry Cu deposit[J]. Geochem. Explor. Environ. Anal. 20 (4), 480–495. <https://doi.org/10.1144/geochim2020-038>.
- Fu, G., Lu, Q., Yan, J., Farquharson, C.G., Qi, G., Zhang, K., Zhang, Y., Wang, H., Luo, F., 2021. 3D mineral prospectivity modeling based on machine learning: A case study of the Zhuxi tungsten deposit in northeastern Jiangxi Province, South China[J]. Ore Geol. Rev. 131 <https://doi.org/10.1016/j.oregeorev.2021.104010>.
- Ganin, Y., Lempitsky, V., 2014. N4-fields: Neural network nearest neighbor fields for image transforms[J]. Asian Conference on Computer Vision 9004, 536–551.
- Ghezelbash, R., Maghsoudi, A., Carranza, E.J.M., 2020. Sensitivity analysis of prospectivity modeling to evidence maps: Enhancing success of targeting for epithermal gold, Takab district, NW Iran[J]. Ore Geol. Rev. 120 <https://doi.org/10.1016/j.oregeorev.2020.103394>.

- Glorot, X., Bordes, A., Bengio, Y., 2011. Deep Sparse Rectifier Neural Networks[J]. International Conference on Artificial Intelligence and Statistics 15, 315–323.
- Hao, B., Deng, J., Bagas, L., Ge, L., Nie, F., Turner, S., Qing, M., 2016. The Gaosongshan epithermal gold deposit in the Lesser Hinggan Range of the Heilongjiang Province, NE China: Implications for Early Cretaceous mineralization[J]. Ore Geol. Rev. 73, 179–197. <https://doi.org/10.1016/j.oregeorev.2015.03.009>.
- Hassen, I., Gibson, H., Hamzaoui-Azaza, F., Negro, F., Rachid, K., Bouhlila, R., 2016. 3D geological modeling of the Kasserine Aquifer System, Central Tunisia: New insights into aquifer-geometry and interconnections for a better assessment of groundwater resources[J]. J. Hydrol. 539, 223–236. <https://doi.org/10.1016/j.jhydrol.2016.05.034>.
- He, S., Cai, H., Liu, S., Xie, J., Hu, X., 2021. Recovering 3D Basement Relief Using Gravity Data Through Convolutional Neural Networks[J]. Journal of Geophysical Research: Solid Earth 126 (10). <https://doi.org/10.1029/2021jb022611>.
- Jessell, M., 2001. Three-dimensional geological modelling of potential-field[J]. Comput. Geosci. 27, 455–465.
- Khan, U., Zhang, B., Du, J., Jiang, Z., 2021. 3D structural modeling integrated with seismic attribute and petrophysical evaluation for hydrocarbon prospecting at the Dhulian Oilfield, Pakistan[J]. Front. Earth Sci. 15 (3), 649–675. <https://doi.org/10.1007/s11707-021-0881-1>.
- Kingma DP, Ba JL. 2015. Adam: A method for stochastic optimization[A].// 3rd International Conference on Learning Representations, ICLR 2015, May 7, 2015 - May 9, 2015[A], San Diego, CA, United states: International Conference on Learning Representations, ICLR.
- Krizhevsky, A., Sutskever, I., Hinton, G.E., 2017. ImageNet classification with deep convolutional neural networks[J]. Commun. ACM 60 (6), 84–90. <https://doi.org/10.1145/3065386>.
- Lange J, Cavallaro G, Götz M, Erlingsson E, Riedel M. 2018. The influence of sampling methods on pixel-wise hyperspectral image classification with 3D convolutional neural network[J]. IEEE International Symposium on Geoscience and Remote Sensing IGARSS: 2087 - 2090.
- Le QV, Monga MARR, Chen MDK, Dean GSCJ, Ng AY. 2013. Building High-level Features Using Large Scale Unsupervised Learning[J]. The 29th International Conference on International Conference on Machine Learning: 507–514.
- Lecun, Y., Bottou, L., Bengio, Y., Haffner, P., 1998. Gradient-Based Learning Applied to Document Recognition[J]. IEEE 86 (11), 2278–2324.
- LeCun, Y., Bengio, Y., Hinton, G., 2015. Deep learning[J]. Nature 521 (7553), 436–444. <https://doi.org/10.1038/nature14539>.
- LeCun, Y.A., Bottou, L., Orr, G.B., Müller, K.-R., 2012. Efficient backprop[J]. Lect. Notes Comput. Sci 7700, 9–48.
- Li, S., Chen, J., Liu, C., Wang, Y., 2021. Mineral Prospectivity Prediction via Convolutional Neural Networks Based on Geological Big Data[J]. J. Earth Sci. 32 (2), 327–347. <https://doi.org/10.1007/s12583-020-1365-z>.
- Li X, Sun X, Meng Y, Liang J, Wu F, Li J. 2020. Dice Loss for Data-imbalanced NLP Tasks [J]. 58th Annual Meeting of the Association for Computational Linguistics, 58: 465–476.
- Li, H., Li, X., Yuan, F., Jowitt, S.M., Zhang, M., Zhou, J., Zhou, T., Li, X., Ge, C., Wu, B., 2020. Convolutional neural network and transfer learning based mineral prospectivity modeling for geochemical exploration of Au mineralization within the Guandian-Zhangbaling area, Anhui Province, China[J]. Appl. Geochem. 122 (1), 104747 <https://doi.org/10.1016/j.apgeochem.2020.104747>.
- Li, H., Li, X., Yuan, F., Zhang, M., Li, X., Ge, C., Wang, Z., Guo, D., Lan, X., Tang, M., Lu, S., 2023. Genetic Algorithm Optimized Light Gradient Boosting Machine for 3D Mineral Prospectivity Modeling of Cu Polymetallic Skarn-Type Mineralization, Xuancheng Area, Anhui Province, Eastern China[J]. Nat. Resour. Res. 32 (5), 1897–1916. <https://doi.org/10.1007/s11053-023-10227-y>.
- Li, N., Song, X., Li, C., Xiao, K., Li, S., Chen, H., 2019. 3D Geological Modeling for Mineral System Approach to GIS-Based Prospectivity Analysis: Case Study of an MVT Pb-Zn Deposit[J]. Nat. Resour. Res. 28 (3), 995–1019. <https://doi.org/10.1007/s11053-018-9429-9>.
- Li, N., Yin, S., Li, C., Wang, Y., Xiao, K., Cao, R., Hua, W., Chu, W., Song, X., Li, C., 2023. An Uncertainty Analysis Method Based on a Globally Optimal Truth Discovery Model for Mineral Prospectivity Mapping[J]. Math. Geosci. <https://doi.org/10.1007/s11004-023-10086-6>.
- Li, X., Yuan, F., Zhang, M., Jia, C., Jowitt, S.M., Ord, A., Zheng, T., Hu, X., Li, Y., 2015. Three-dimensional mineral prospectivity modeling for targeting of concealed mineralization within the Zhonggu iron orefield, Ningwu Basin, China[J]. Ore Geol. Rev. 71, 633–654. <https://doi.org/10.1016/j.oregeorev.2015.06.001>.
- Li, X., Zhou, N., Xie, X., 2018. Reservoir characteristics and three-dimensional architectural structure of a complex fault-block reservoir, beach area, China[J]. J. Pet. Explor. Prod. Technol. 8 (4), 1535–1545. <https://doi.org/10.1007/s13202-018-0433-8>.
- Li, X., Yuan, F., Zhang, M., Jowitt, S.M., Ord, A., Zhou, T., Dai, W., 2019. 3D computational simulation-based mineral prospectivity modeling for exploration for concealed Fe-Cu skarn-type mineralization within the Yueshan orefield, Anqing district, Anhui Province, China[J]. Ore Geol. Rev. 105, 1–17. <https://doi.org/10.1016/j.oregeorev.2018.12.003>.
- Li, X., Xue, C., Chen, Y., Yuan, F., Li, Y., Zheng, C., Zhang, M., Ge, C., Guo, D., Lan, X., Tang, M., Lu, S., 2023. 3D convolutional neural Network-based 3D mineral prospectivity modeling for targeting concealed mineralization within Chating area, middle-lower Yangtze River metallogenic Belt, China[J]. Ore Geol. Rev. 157 <https://doi.org/10.1016/j.oregeorev.2023.105444>.
- Lin, T.-Y., Goyal, P., Girshick, R., He, K., Dollar, P., 2017. Focal Loss for Dense Object Detection[J]. In: IEEE International Conference on Computer Vision (ICCV), pp. 2980–2988.
- Lindsay, M.D., Aillères, L., Jessell, M.W., de Kemp, E.A., Betts, P.G., 2012. Locating and quantifying geological uncertainty in three-dimensional models: Analysis of the Gippsland Basin, southeastern Australia[J]. Tectonophysics 546–547, 10–27. <https://doi.org/10.1016/j.tecto.2012.04.007>.
- Liu, J., Bai, X., Zhao, S., Tran, M., Zhang, Z., Zhao, Z., Zhao, H., Lu, J., 2011. Geology of the Sandaowanzi telluride gold deposit of the northern Great Xing'an Range, NE China: Geochronology and tectonic controls[J]. J. Asian Earth Sci. 41 (2), 107–118. <https://doi.org/10.1016/j.jseas.2010.12.011>.
- Liu, Y., Li, W., Feng, Z., Wen, Q., Neubauer, F., Liang, C., 2017. A review of the Paleozoic tectonics in the eastern part of Central Asian Orogenic Belt[J]. Gondw. Res. 43, 123–148. <https://doi.org/10.1016/j.gr.2016.03.013>.
- Liu, C., Zhou, Z., Wang, G., Wu, C., Li, H., Zhu, Y., Jiang, T., Liu, W., Ye, B., Liu, Y., 2017. Geochronology and geochemistry of the Late Jurassic bimodal volcanic rocks from Hailesen area, central-southern Great Xing'an Range, Northeast China[J]. Geol. J. 53 (5), 2099–2117. <https://doi.org/10.1002/gj.3036>.
- Mohammadpour, M., Bahroodi, A., Abedi, M., 2021. Three dimensional mineral prospectivity modeling by evidential belief functions, a case study from Kahang porphyry Cu deposit[J]. J. Afr. Earth Sc. 174 <https://doi.org/10.1016/j.jafrearsci.2020.104098>.
- Pinheiro, P.H., Collobert, R., 2014. Recurrent Convolutional Neural Networks for Scene Labeling[J]. In: International Conference on Machine Learning, p. 32.
- Polyak, B.T., 1964. Some methods of speeding up the convergence of iteration methods [J]. USSR Comput. Math. Math. Phys. 4 (5), 1–17. [https://doi.org/10.1016/0041-5553\(64\)90137-5](https://doi.org/10.1016/0041-5553(64)90137-5).
- Qin, Y., Liu, L., Wu, W., 2021. Machine Learning-Based 3D Modeling of Mineral Prospectivity Mapping in the Anqing Orefield, Eastern China[J]. Nat. Resour. Res. 30 (5), 3099–3120. <https://doi.org/10.1007/s11053-021-09893-7>.
- Rezaei, A., Hassani, H., Moarefvand, P., Golmohammadi, A., Jabbari, N., 2022. Three-dimensional Subsurface Modeling and Classification of Mineral Reserve: A Case Study of the C-North Iron Skarn Ore Reserve, Sangan, NE Iran[J]. Arab. J. Geosci. 15 (4) <https://doi.org/10.1007/s12517-022-09625-y>.
- Ruder S (2016) “An overview of gradient descent optimization algorithms.” arXiv: 1609.04747. DOI: 10.48550/arXiv.1609.04747.
- Sergey I, Christian S. 2015. Batch Normalization Accelerating Deep Network Training by Reducing Internal Covariate Shift[J]. International Conference on Machine Learning, 37.
- Ruopp, M.D., Perkins, N.J., Whitcomb, B.W., Schisterman, E.F., 2008. Youden Index and Optimal Cut-Point Estimated from Observations Affected by a Lower Limit of Detection[J]. Biom. J. 50, 419–430. <https://doi.org/10.1002/bimj.200710415>.
- Simonyan, K., Zisserman, A., 2015. Very Deep Convolutional Networks for Large-Scale Image Recognition[J]. Cornell University Library arXiv.org, 2331–8422.
- Tieleman T, Hinton G (2012). Lecture 6.5-rmsprop: Divide the gradient by a running average of its recent magnitude, google.
- Vollgger, S.A., Cruden, A.R., Aillères, L., Cowan, E.J., 2015. Regional dome evolution and its control on ore-grade distribution: Insights from 3D implicit modelling of the Navachab gold deposit, Namibia[J]. Ore Geol. Rev. 69, 268–284. <https://doi.org/10.1016/j.oregeorev.2015.02.020>.
- Wang, G., Li, R., Carranza, E.J.M., Zhang, S., Yan, C., Zhu, Y., Qu, J., Hong, D., Song, Y., Han, J., Ma, Z., Zhang, H., Yang, F., 2015. 3D geological modeling for prediction of subsurface Mo targets in the Luanchuan district, China[J]. Ore Geol. Rev. 71, 592–610. <https://doi.org/10.1016/j.oregeorev.2015.03.002>.
- Wang, L., Qin, K., Song, G., Pang, X., Li, Z., Zhao, C., Jin, L., Zou, X., Li, G., 2018. Volcanic-subvolcanic rocks and tectonic setting of the Zhengguan intermediate sulfidation epithermal Au-Zn deposit, eastern Central Asian Orogenic Belt, NE China [J]. J. Asian Earth Sci. 165, 328–351. <https://doi.org/10.1016/j.jseaes.2018.07.023>.
- Wang, L.F., Wu, X.B., Zhang, B.Y., Li, X.F., Huang, A.S., Meng, F., Dai, P.Y., 2019. Recognition of Significant Surface Soil Geochemical Anomalies Via Weighted 3D Shortest-Distance Field of Subsurface Orebodies: A Case Study in the Hongtoushan Copper Mine, NE China[J]. Nat. Resour. Res. 28 (3), 587–607. <https://doi.org/10.1007/s11053-018-9410-7>.
- Wang, G., Zhang, S., Yan, C., Song, Y., Sun, Y., Li, D., Xu, F., 2011. Mineral potential targeting and resource assessment based on 3D geological modeling in Luanchuan region, China[J]. Comput. Geosci. 37 (12), 1976–1988. <https://doi.org/10.1016/j.cageo.2011.05.007>.
- Wang, F., Zhou, X.-H., Zhang, L.-C., Ying, J.-F., Zhang, Y.-T., Wu, F.-Y., Zhu, R.-X., 2006. Late Mesozoic volcanism in the Great Xing'an Range (NE China): Timing and implications for the dynamic setting of NE Asia[J]. Earth Planet. Sci. Lett. 251 (1–2), 179–198. <https://doi.org/10.1016/j.epsl.2006.09.007>.
- Wellmann JF, de la Varga M, Murdie RE, Gessner K, Jessell M (2017). Uncertainty estimation for a geological model of the Sandstone greenstone belt, Western Australia - insights from integrated geological and geophysical inversion in a Bayesian inference framework. Characterization of Ore-Forming Systems from Geological, Geochemical and Geophysical Studies. Gessner K, Blenkinsop TG, Sorjonen-Ward P, London, Geological Society of London: 453–464. DOI: <https://doi.org/10.6084/m9.figshare.c.3899719.v1>.
- Xiang, J., Xiao, K., Carranza, E.J.M., Chen, J., Li, S., 2019. 3D Mineral Prospectivity Mapping with Random Forests: A Case Study of Tongling, Anhui, China[J]. Nat. Resour. Res. 29 (1), 395–414. <https://doi.org/10.1007/s11053-019-09578-2>.
- Xu, Y., Li, Z., Xie, Z., Cai, H., Niu, P., Liu, H., 2021. Mineral prospectivity mapping by deep learning method in Yawan-Daqiao area, Gansu[J]. Ore Geol. Rev. 138, 104316. <https://doi.org/10.1016/j.oregeorev.2021.104316>.
- Zeiler MD (2012) “ADADELTA: An Adaptive Learning Rate Method.” arXiv:1212.5701. DOI: 10.48550/arXiv.1212.5701.
- Zhang, S., Carranza, E.J.M., Wei, H., Xiao, K., Yang, F., Xiang, J., Zhang, S., Xu, Y., 2021. Data-driven Mineral Prospectivity Mapping by Joint Application of Unsupervised Convolutional Auto-encoder Network and Supervised Convolutional Neural Network

- [J]. Nat. Resour. Res. 30 (2), 1011–1031. <https://doi.org/10.1007/s11053-020-09789-y>.
- Zhang, B., Chen, Y., Huang, A., Lu, H., Cheng, Q., 2018. Geochemical field and its roles on the 3D prediction of concealed ore-bodies.pdf[J]. Acta Petrol. Sin. 34 (2), 352–362.
- Zhang, Q., Chen, J., Xu, H., Jia, Y., Chen, X., Jia, Z., Liu, H., 2022. Three-Dimensional Mineral Prospective Mapping by XGBoost Modeling: A Case Study of the Lannigou Gold Deposit, China[J]. Nat. Resour. Res. 31 (3), 1135–1156. <https://doi.org/10.1007/s11053-022-10054-7>.
- Zhang, B., Du, L., Khan, U., Tong, Y., Wang, L., Deng, H., 2023. AdaHRBF v1.0: gradient-adaptive Hermite-Birkhoff radial basis function interpolants for three-dimensional stratigraphic implicit modeling[J]. Geosci. Model Dev. 16 (13), 3651–3674. <https://doi.org/10.5194/gmd-16-3651-2023>.
- Zhang, Z., Mao, J., Wang, Y., Pirajno, F., Liu, J., Zhao, Z., 2010. Geochemistry and geochronology of the volcanic rocks associated with the Dong'an adularia-sericitic epithermal gold deposit, Lesser Hinggan Range, Heilongjiang province, NE China: Constraints on the metallogenesis[J]. Ore Geol. Rev. 37 (3–4), 158–174. <https://doi.org/10.1016/j.oregeorev.2010.03.001>.
- Zhang, R., Quan, W., Wu, B., Li, Z., Yan, D.M., 2020. Pixel-wise Dense Detector for Image Inpainting[J]. Comput. Graphics Forum 39 (7), 471–482. <https://doi.org/10.1111/cgf.14160>.
- Zhang, C., Wang, E., Bi, Z., Han, R., Shao, J., Liu, B., Chen, J., Zeng, N., 2019. Geochronology and isotope geochemistry studies of an epithermal gold deposit in the northern Lesser Khingan Range, NE China: The Gaosongshan example[J]. Ore Geol. Rev. 105, 356–374. <https://doi.org/10.1016/j.oregeorev.2019.01.001>.
- Zhang, Z., Wang, G., Liu, C., Cheng, L., Sha, D., 2021. Bagging-based positive-unlabeled learning algorithm with Bayesian hyperparameter optimization for three-dimensional mineral potential mapping[J]. Comput. Geosci. 154, 104817 <https://doi.org/10.1016/j.cageo.2021.104817>.
- Zhang, N., Zhou, K., Batyrshin, I., Pamučar, D.S., Crippa, P., Liu, F., 2015. Mineral prospectivity mapping with weights of evidence and fuzzy logic methods[J]. J. Intell. Fuzzy Syst. 29 (6), 2639–2651. <https://doi.org/10.3233/ifs-151967>.
- Zheng, Y., Deng, H., Wu, J., Wang, R., Liu, Z., Wu, L., Mao, X., Chen, J., 2023. Space-associated domain adaptation for three-dimensional mineral prospectivity modeling [J]. Int. J. Digital Earth 16 (1), 2885–2911. <https://doi.org/10.1080/17538947.2023.2241432>.
- Zuo, R., Xiong, Y., 2017. Big Data Analytics of Identifying Geochemical Anomalies Supported by Machine Learning Methods[J]. Nat. Resour. Res. 27 (1), 5–13. <https://doi.org/10.1007/s11053-017-9357-0>.
- Zuo, R., Xiong, Y., Wang, J., Carranza, E.J.M., 2019. Deep learning and its application in geochemical mapping[J]. Earth Sci. Rev. 192, 1–14. <https://doi.org/10.1016/j.earscirev.2019.02.023>.